Remote Sens. Environ., 263, (2021), p. 112570
10.1016/j.rse.2021.112570

Modelling hyperspectral- and thermal-based plant traits for the early detection of *Phytophthora*-induced symptoms in oak decline

A. Hornero[a,b*], P.J. Zarco-Tejada[c,b], J.L. Quero[d], P.R.J. North[a], F.J. Ruiz-Gómez[d], R. Sánchez-Cuesta[d], R. Hernandez-Clemente[a].

[a]Department of Geography, Swansea University, SA2 8PP Swansea, United Kingdom
[b]Instituto de Agricultura Sostenible (IAS), Consejo Superior de Investigaciones Científicas (CSIC), Avenida Menéndez Pidal s/n, 14004 Córdoba, Spain
[c]School of Agriculture and Food, Faculty of Veterinary and Agricultural Sciences (FVAS), and Department of Infrastructure Engineering, Faculty of Engineering and Information Technology (FEIT), University of Melbourne, Melbourne, Victoria, Australia
[d]Departamento de Ingeniería Forestal, Laboratorio de Ecofisiología de Sistemas Forestales ECSIFOR—ERSAF, Universidad de Córdoba, Campus de Rabanales, Crta, IV, km. 396, E-14071 Córdoba, Spain

[*]*Corresponding author*

Abstract

Holm oak decline is a complex phenomenon mainly influenced by the presence of *Phytophthora cinnamomi* and water stress. Plant functional traits (PTs) are altered during the decline process — initially affecting the physiological condition of the plants with non-visual symptoms and subsequently the leaf pigment content and canopy structure — being its quantification critical for the development of scalable detection methods for effective management. This study examines the relationship between spectral-based PTs and oak decline incidence and severity. We evaluate the use of high-resolution hyperspectral and thermal imagery (< 1 m) together with a 3-D radiative transfer model (RTM) to assess a supervised classification model of holm oak decline. Field surveys comprising more than 1100 trees with varying disease incidence and severity were used to train and validate the model and predictions. Declining trees showed decreases of model-based PTs such as water, chlorophyll, carotenoid, and anthocyanin contents, as well as fluorescence and leaf area index, and increases in crown temperature and dry matter content, compared to healthy trees. Our classification model built using different PT indicators showed up to 82% accuracy for decline detection and successfully identified 34% of declining trees that were not detected by visual inspection and confirmed in a re-evaluation 2 years later. Among all variables analysed, canopy temperature was identified as the most important variable in the model, followed by chlorophyll fluorescence. This methodological approach

identified spectral plant traits suitable for the detection of pre-symptomatic trees and mapping of oak forest disease outbreaks up to 2 years in advance of identification via field surveys. Early detection can guide management activities such as tree culling and clearance to prevent the spread of dieback processes. Our study demonstrates the utility of 3-D RTM models to untangle the PT alterations produced by oak decline due to its heterogeneity. In particular, we show the combined use of RTM and machine learning classifiers to be an effective method for early detection of oak decline potentially applicable to many other forest diseases worldwide.

Keywords: High-resolution imagery, radiative transfer modelling, forest dieback, disease monitoring.

1. Introduction

Plant functional traits (PTs), such as biochemical composition, chlorophyll fluorescence, water and dry matter content, crown temperature, and vegetation structure, are closely linked to plant health conditions and the responses to environmental and biotic stressors (Ahrens *et al.*, 2020). Changes in PTs may alert managers to biotic and abiotic stressors and thus enable timely management interventions (Cunniffe *et al.*, 2016). Hyperspectral signatures of plants provide an efficient alternative to standard field surveys by enabling monitoring of vegetation status (including biochemical and functional assessments) over large areas at a reduced cost (Homolová *et al.*, 2013; Rocha *et al.*, 2019). Recent studies provide evidence that the quantification of PTs from hyperspectral and thermal images can successfully detect pre-visual symptoms of harmful crop pathogens, such as *Xylella fastidiosa* (*Xf*) infection in olive trees (Zarco-Tejada *et al.*, 2018).

Retrieving PTs from spectra obtained in non-agricultural contexts, such as forest canopies, is challenging because of their high variability. Natural forests, for example, are highly heterogenous in species composition and canopy structure, resulting in spectral mixture effects produced by forest canopy structure, shadows, and understory. Furthermore, they may have high levels of intraspecific variability, driven by microsite and ecophysiological conditions (Fernández i Marti *et al.*, 2018; Navarro-Cerrillo *et al.*, 2018). The spectral mixing produced in heterogeneous forest canopies reduces the accuracy of PTs retrieved from images, especially those derived from narrow regions of the spectrum such as the chlorophyll fluorescence emission region (Hernández-Clemente *et al.*, 2017).

Forest decline is a pervasive decrease of forest health resulting from a complex interaction of a potentially large number of biotic and abiotic factors (Hutchings *et al.*, 2000), including stresses such as water deficit, air pollution, and invasive pests (Manion and Lachance, 1992; Trumbore *et al.*, 2015). In the case of oak decline on the Iberian Peninsula, water stress and root rot caused by *Phytophthora cinnamomi* (*Pc*) and related oomycetes are thought to be the main drivers of tree death (Ruiz-Gómez *et al.*, 2019). This pathogen is one of the most pervasive invasive alien species in forest ecosystems of the northern hemisphere (Burgess *et al.*, 2017). It is a challenge to identify the relationship between water stress and root rot. But it has been observed that the reduction in water availability caused by water stress increases susceptibility to *Pc* infection (Corcobado *et al.*, 2013). Infected trees exhibit regressive decline immediately after showing visual symptoms such as defoliation, crown or canopy discolouration, and brown foliage remaining attached to the canopy (Camilo-Alves *et al.*,

2013). After these symptoms are detected, there is no opportunity for forest management to prevent tree death. For this reason, it is critical to developing accurate methods for the early detection of oak decline that maximises the effectiveness of silvicultural treatments such as calcium soil fertilisers, biofumigant crops, or fosetyl-aluminium treatments (Romero *et al.*, 2019). Understanding the early phase as a pre-symptomatic or non-symptomatic stage, where trees may be affected but have not yet developed symptoms.

Several spectral-based strategies have been developed to quantify critical PTs in natural forest canopies, as recently reviewed by Hernández-Clemente *et al.* (2019). Methodologies range from those based on empirical relationships between field observations and specific spectral bands or vegetation indices (VIs) to approaches involving 3-D radiative transfer models (RTMs) or machine learning (ML) techniques. While empirical relationships can be readily developed for a wide range of traits of interest, 3-D RTM requires significant computational effort. A main disadvantage of the empirical approach is its limited generalisability to different spatial and temporal contexts. By contrast, RTMs are causal models robust to variations in geometry, illumination, and scene components (i.e., canopy, understory, soil), helping incorporate context dependency and enabling generalisation to different environments. These properties are important for deriving PTs from forest canopies, where 3-D RTMs such as FLIGHT (North, 1996) or DART (Gastellu-Etchegorry *et al.*, 1996) represent the spatial heterogeneity of forest canopies fairly effectively (Hernández-Clemente *et al.*, 2017, 2012; Kötz *et al.*, 2004; Liu *et al.*, 2020; Roberts *et al.*, 2020). A recent study using FLIGHT8 has shown the need to account for effects of shrub and/or grass understories in addition to tree canopies in quantifying variables such as chlorophyll fluorescence (Hornero *et al.*, 2021).

A semi-causal method is the combined use of PTs retrieved with RTMs and VIs (Zarco-Tejada *et al.*, 2018). Numerous VIs have been formulated and tested for quantifying biomass loss related to advanced stages of plant diseases (Castrignano *et al.*, 2020). Some formulations, such as the soil-adjusted vegetation index (SAVI) or the modified chlorophyll absorption ratio index (MCARI), have been shown to minimise the background and atmospheric effects and perform better for forest canopies than traditional formulations such as NDVI (Hornero *et al.*, 2020). Zarco-Tejada *et al.* (2001) demonstrated that a red edge spectral index, R_{750}/R_{710}, reduced forest shadow effects better than other standard chlorophyll indicators used to estimate chlorophyll *a* and *b* content.

The diagnosis of plant diseases requires quantifying not only forest biomass but also the physiological condition of that biomass (Cunniffe *et al.*, 2016). Functional PTs such as photosynthetic rate, water stress, leaf anthocyanin, chlorophyll *a* and *b*, and carotenoid content may be used for early detection of diseases (Hernández-Clemente *et al.* 2019). Also, a group of carotenoids, the xanthophyll cycle carotenoids, plays a photoprotective role, preventing damage from excess light to photosynthetic systems, and are potentially detected through the photochemical reflectance index (PRI), thus serving as a proxy for forest health (Hernández-Clemente *et al.*, 2011; Sims and Gamon, 2002). Other useful indicators of plant health include sun-induced chlorophyll fluorescence (SIF) emission and canopy temperature, which are often used as powerful non-invasive markers to track the status, resilience, and recovery of vegetation (Gonzalez-Dugo *et al.*, 2014; Mohammed *et al.*, 2019; Zarco-Tejada *et al.*, 2012).

However, the relative importance of different PT indicators for detecting disease remains largely unknown for many forest species and ecosystems. Understanding the sensitivity of different spectral-based physiological indicators for detecting forest decline in these heterogeneous environments will help guide management and future monitoring campaigns. In this study, we i) expanded our under-

standing of the contributions of different PTs in detecting symptomatic and asymptomatic trees affected by biotic and abiotic stressors in a holm oak forest and ii) used this information to construct a PT-based analytical approach for the early detection and severity assessment of forest decline.

2. Materials and methods

2.1. Study site and field data collection

The study was conducted in an open Mediterranean-like oak savannah or *dehesa* located in Andalusia, southern Spain (37°36′45″ N, 7°21′8″ W, 148 ha, Fig. 1). The dominant species in the forest was holm oak, *Quercus ilex* subsp. *ballota* (Desf.) Samp. Tree density ranged from 30 to 40 trees ha^{-1}. There was an understory of annual plants and typical Mediterranean sclerophyllous and sub-sclerophyllous shrub species, i.e., *Cistus* spp., *Pistacia* spp., *Phillyrea* spp., and *Rosmarinus officinalis*. The climate at the study site is dry thermo-Mediterranean, with mild winters and hot summers, including approximately 120–150 biologically dry days, a mean annual rainfall of 570 mm, and an average annual temperature of 16.8°C, according to the Agroclimatic Information Network of Andalusia (Meteorological Station of Puebla de Guzmán, 37º33′07″ N, 07º14′54″ W). The bedrock is calcareous, and the terrain is characterised by smooth hills (slope <15%). Soils are Eutric Cambisols, Chromic Luvisols, and Lithosols with Dystric Cambisols and Rankers (REDIAM, Junta de Andalucía, 2021). The study area is also affected by the combined effect of water deficiency and erosion, soil compaction, and nutrient losses (Moralejo *et al.*, 2009).

Two field surveys were conducted in the study site in summer 2017 and summer 2019. During the surveys, disease severity (DS) and disease incidence (DI) were assessed for 1146 individual holm oak trees. Seem (1984) defined DS as the quantity of disease affecting entities within a sampling unit; DI is a quantal measure, defined as the proportion or percentage of diseased entities within a sampling unit. DS thus accounts for disease severity, while DI considers only whether a tree is affected or not.

Based on visual inspection, we assigned individual trees to one of the four DS categories available (Fig. 2) depending on the proportion of the crown affected by defoliation (Eichhorn *et al.*, 2017) and other typical *Pc*-induced symptoms, including dead branches in the crown, stem cankers, and adventitious epicormic sprouts (Jung *et al.*, 2000). DS ranged from 0, indicating the absence of visual symptoms, to 3, in which most of the branches in the crown were dead, following the classification of the Andalusian Forest Damage Monitoring Network (Consejería de Medio Ambiente y Ordenación del Territorio, 2018) (Table 1; Fig. 2). According to this classification, defoliation refers to both reduced leaf retention and premature loss compared to regular tree growth cycles. The part of the crown that is evaluated includes all live branches and thin branches that are dead but still bear leaves. However, it excludes thick branches that have been dead for years and have already lost their natural buds, epicormic shoots below the crown, and gaps in the crown where branches have never existed. DI was either 0 or 1, indicating non-symptomatic trees and symptomatic trees, respectively, where non-symptomatic trees corresponded to a DS of 0 and symptomatic trees to any other severity (DS ≥ 1).

The presence of *Pc* on holm oak roots was confirmed through molecular analyses in the study area. Soil samples were collected on three different trees located in the centre of the study area. The analysis and the results are detailed in Ruiz-Gómez *et al.* (2019).

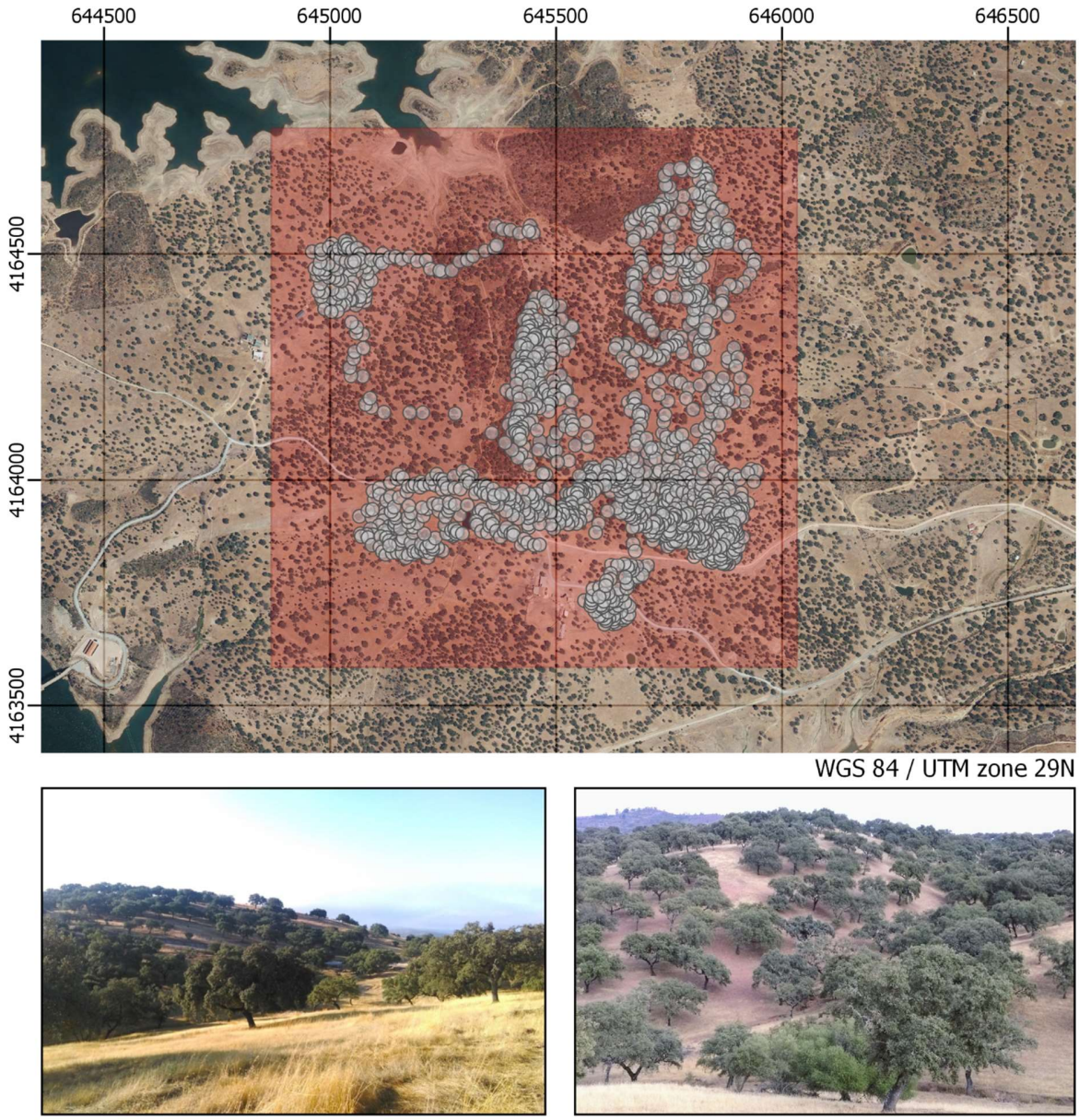

Figure 1. Location of the study site selected for PT retrieval through high-resolution imaging (top). The square shaded in red represents the area of the field survey, and the grey dots indicate individual evaluation. Photographs illustrating the heterogeneity of the landscape within the study area are shown below.

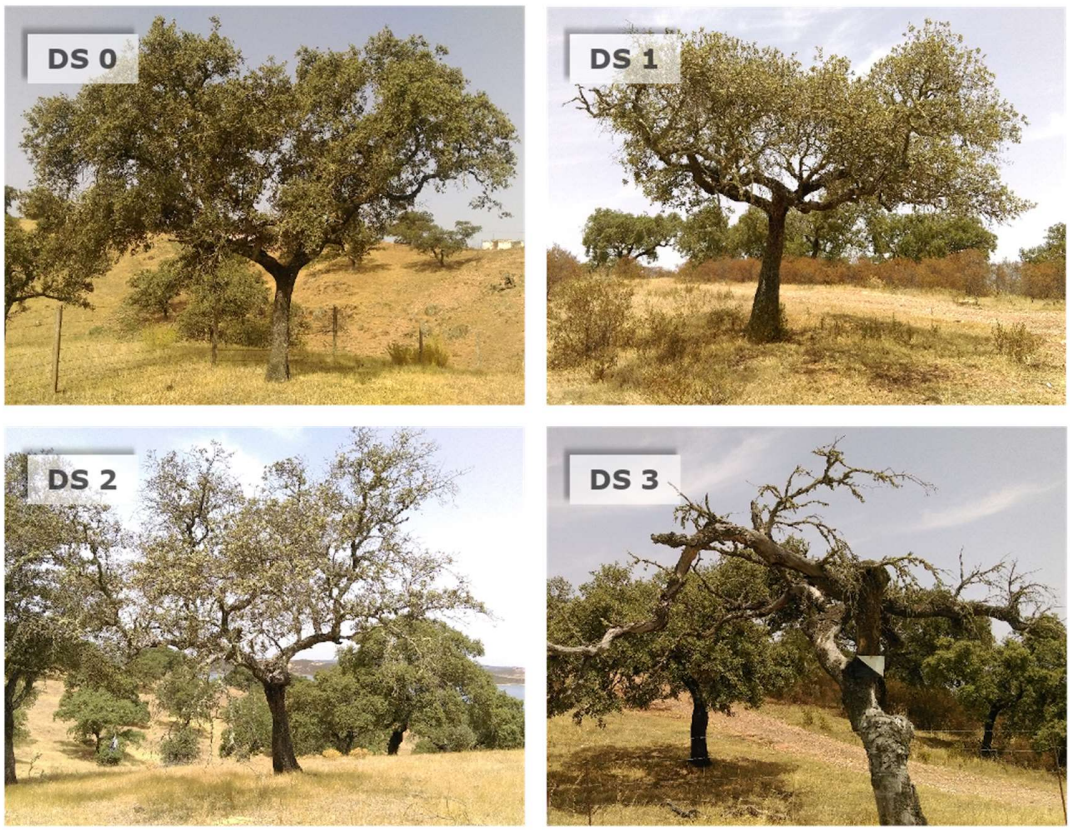

Figure 2. Examples of the four forest disease severity (DS) levels assigned to holm oak trees ($N = 1146$) during a field survey in 2017, which was repeated in 2019. The classes range from apparently healthy trees (DS = 0) to trees whose canopies show a prevalence of dead branches (DS = 3).

Table 1
Forest health condition assessment: crown-level severity and incidence levels.

DS Level	Severity	Description	Defoliation	Incidence
0	Healthy	Symptomless or low symptom incidence	0–15%	No incidence
1	Low to moderate severity	Low to moderate defoliation and no or few additional symptoms affecting a limited part of the canopy	15–50%	Incidence
2	Medium to high severity	Medium to high defoliation of the crown and several additional symptoms	50–85%	Incidence
3	High to extreme severity	High defoliation uniformly distributed all over the crown, totally defoliated trees, and additional symptoms	85–100%	Incidence

2.1.1 Leaf pigment quantification

Biochemical measurements were taken on leaves from 15 selected trees in the study area in the summers of 2013, 2015, and 2017, in which the chlorophyll (C_{ab}), carotenoid (C_{ar}), and anthocyanin (A_{nth}) contents were measured (Table 2). Leaf pigment content was measured by destructive methods on 12 samples per tree (three biological replicates per orientation, i.e., North, East, South, and West). Samples were collected from the sunlit branches at the top of the crown during a 1-hour window around solar noon. Leaves were immediately frozen in liquid nitrogen in the field and kept below –20°C until the analysis of pigment concentration was performed in the laboratory. Photosynthetic pigment extracts (chlorophylls and carotenoids) were obtained from a mixture of 2-cm^2 ground leaf material per sample (four discs of 0.5 cm^2); the leaves were milled in a mortar bed on ice with liquid nitrogen and diluted in acetone to 5 mL (in the presence of sodium ascorbate). Extracts were then filtered through a 0.45-µm PTFE hydrophobic filter to separate pigment extracts from remaining fractions. Extractions and measurements were performed under reduced light conditions to avoid degradation of the pigments, with five technical replications conducted per biological sample. Photosynthetic pigment quantification was done through absorbance measurement after separation by high-precision liquid chromatography (HPLC) following the methodology detailed by Hernández-Clemente *et al.* (2012).

Anthocyanins were extracted by suspending two 0.5-cm^2 leaf discs in acidic solution (methanol 1% HCl) following Murray and Hackett (1991). The absorbance of anthocyanins (AAs) in the samples was calculated by subtracting 24% of the maximum absorbance of chlorophylls (653 nm) from the maximum absorbance of the anthocyanins (532 nm) (1)

$$\mathrm{AA} = A_{532} - 0.24A_{653} \qquad (1)$$

Concentrations were estimated using a molar extinction coefficient of 30 mL mol^{-1} cm^{-1} (Steele *et al.*, 2009). Five technical replicates were performed for each biological sample, and results are shown in units of µg cyanidin-3-glucoside equivalents per cm^2 (Lee *et al.*, 2008).

2.1.2 Plant functional traits

Steady-state leaf fluorescence (F_s) was measured for 15 trees using 12 leaves per tree (three per orientation) with a FluorPen FP100 (Photon Systems Instruments, Drásov, Czech Republic). These measurements were used as a proxy of the airborne SIF retrievals and a field-level assessment of plant functional stress for each severity level.

In July 2013, the leaf area index (LAI) was measured using an LAI-2000 Plant Canopy Analyzer (LI-COR, Inc., Lincoln, NE, USA) for the same 15 trees as above. At each tree, the device was placed with the optical sensor in eight different orientations under the canopy, 1 m above the ground, and using a 90° view-restricting cap. Measurements for LAI estimation included a reference reading above the canopy and several readings below the canopy. All measurements were made at dawn. The coordinates for all trees (both sampled and visually scored) were recorded using a GPS (Garmin GPSMAP 64s) device with a spatial accuracy below 3 m.

Table 2
Summary of field measurements and surveys

Year	Tree-health field survey	C_{ab}	C_{ar}	A_{nth}	F_s	LAI
2013		✓	✓	✓	✓	✓
2015		✓	✓		✓	
2017	✓	✓	✓		✓	
2019	✓					

C_{ab}: chlorophyll *a* + *b* content; C_{ar}: carotenoids; A_{nth}: anthocyanins; F_s: steady-state leaf fluorescence; LAI: leaf area index.

2.2. Airborne hyperspectral and thermal imagery

2.2.1. High-resolution image data collection

We collected high-resolution images on 19 July 2017 using a visible near-infrared (VIS-NIR) hyperspectral imager (Hyperspec model, Headwall Photonics Inc., Fitchburg, MA, USA), a hyperspectral sensor covering NIR and short-wave infrared (SWIR) regions (Hyperspec NIR-100, Headwall Photonics), and a thermal camera (FLIR SC655, FLIR Systems, Wilsonville, OR, USA) installed in tandem onboard a Cessna aircraft operated by the Laboratory for Research Methods in Quantitative Remote Sensing (QuantaLab), Spanish National Research Council (CSIC). The imagery was acquired at 350 m above ground level with the aircraft flying on the solar plane, with a track width of 185 m, resulting in 720 ha of ground surface covered (Fig. 3). The VIS-NIR camera operated with 260 spectral bands (400–885 nm) and a radiometric resolution of 12 bits at a 1.865-nm centre wavelength (CWL) interval, yielding 6.4-nm full-width at half-maximum (FWHM) spectral resolution with a 25-µm slit. The acquisition frame rate on board the aircraft was 50 frames per second with an integration time of 18 ms. The focal length was 8 mm, producing an angular field of view (FOV) of 49.82°. The images derived from this sensor resulted in a ground resolution of 60 cm, allowing us to distinguish individual oak tree crowns from the background. Further details regarding the platform and sensor configuration can be found in Zarco-Tejada *et al.* (2013). The NIR-SWIR sensor was operated with 165 spectral bands (950–1750 nm), yielding 6.05 nm FWHM (25-µm slit size) and 16-bit radiometric resolution. The sensor was configured with an acquisition rate of 25 fps with an integration time of 40 ms. The 12.5-mm-focal-length lens resulted in an angular FOV of 38.6°, with a 90 cm/px spatial resolution. The FWHM and the centre wavelength for each spectral band were derived after spectral calibration using a monochromator (Cornerstone 260 1/4 m, model 74100, Newport Oriel Instrument, CA, USA) and an XE-1 Xenon calibration light source (Ocean Optics, USA).

The thermal sensor (FLIR SC655, FLIR Systems, Inc., USA) had a resolution of 640 × 480 pixels and was connected to an acquisition board via the Gigabit Ethernet protocol. It was equipped with a 24.5-mm F-number 1.0 lens providing an angular FOV of 45 × 33.7°. The detector is a focal plane array uncooled microbolometer and has a spectral range from 7.5 to 14 µm. This camera is equipped with a thermoelectric cooling (TE) stabilisation system, which enables a thermal sensitivity below 50 mK. The characteristics of the sensors on board, as well as their specific setup in this study, are detailed in Table 3.

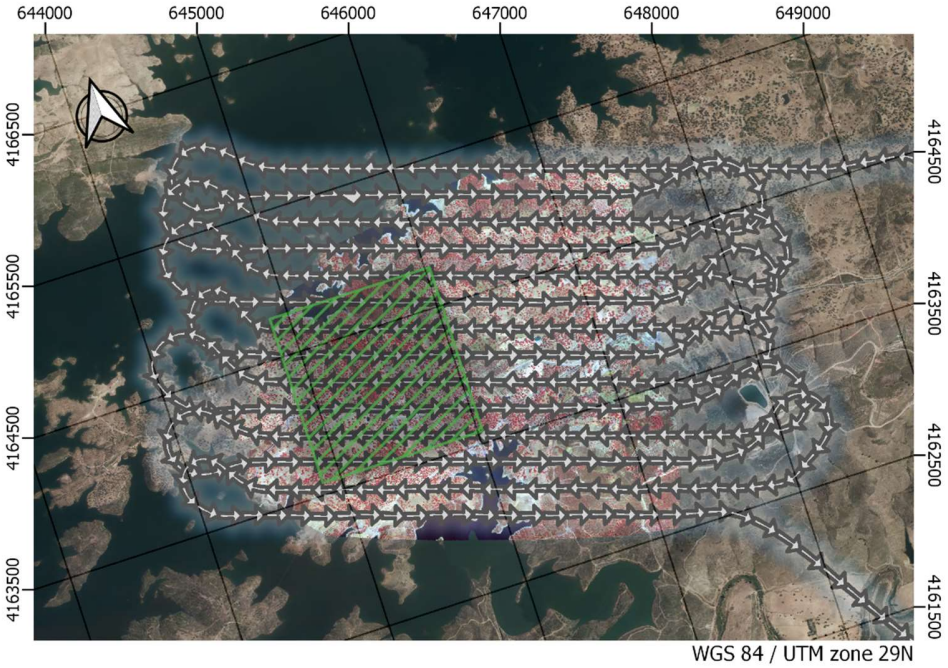

Figure 3. Flight path for image acquisition. White arrows and line indicate the flight path and the hashed green square is framed over the study area. The background shows the VIS-NIR hyperspectral mosaic, overlaid on an orthophoto from the Spanish National Geographic Institute (IGN, OrtoPNOA 2017 CC-BY 4.0)

Table 3
Technical characteristics of the airborne imaging sensors and operational settings

	Hyperspectral		Thermal
	VNIR	NIR-100	SC655
Wavelength range (µm)	0.4–0.885	0.95–1.75	7.5–14
Spectral bands	260	165	1
Spatial bands	1004	320	640 × 480
Focal plane array detector	Silicon CCD	InGaAs	VOx
TE cooling	No	Yes	Yes
Detector pixel pitch (µm)	7.4	12	17
FWHM (nm)	6.4	6.05	–
Slit size (µm)	25	25	–
Radiometric resolution (bits)	12	16	16
Integration time (ms)	18	40	8
Frame period (ms)	55.55	18	1000
Aperture	F/1.4	F/2.0	F/1.0
Focal length (mm)	8	12.5	24.5
Spatial resolution (cm/px)	60	90	60
FOV (deg)	49.82	38.6	45 × 33.7
Communication protocol	CameraLink	USB	GigE

2.2.2. Image post-processing

Both hyperspectral sensors were radiometrically calibrated by means of an integrating sphere (Uniform Source System, model CSTM-USS-2000C, Labsphere Inc., North Sutton, NH, USA) using coefficients derived from the calibrated light source at four constant levels of illumination. Atmospheric correction for the VIS-NIR sensor was performed using the total incoming radiance measured with a field spectroradiometer (ASD HandHeld Pro, Malvern Panalytical Ltd, Malvern, England). Atmospheric correction was simulated with the SMARTS model (Gueymard, 1995, 2001) for the NIR-100 sensor, which allowed the conversion of the radiance images to reflectance for the full range of both sensors. Optical thickness measurements from a Microtops II sunphotometer (Solar Light Co., Philadelphia, PA, USA) and meteorological measurements from a weather station (model WXT510, Vaisala Corporation, Vantaa, Finland) were used as input parameters for the model. Additionally, the effects of illumination and viewing angle were also adjusted using cross-track correction (San and Süzen, 2011) in both hyperspectral processing chains (Fig. 4).

Thermal calibration was conducted in the laboratory using a black body calibration source (LANDCAL model P80P, Land Instruments International Ltd, Dronfield, England) and by indirect calibration using ground temperature measurements with a handheld infrared thermometer (LaserSight from Optris GmbH, Berlin, Germany) as described by Calderón *et al.* (2015) (Fig. 4). Standardised canopy temperature (T_c-T_a) was calculated by subtracting weather station air temperature (T_a) from canopy temperature derived from calibrated thermal imagery (T_c).

Orthorectification of hyperspectral images was performed using PARGE (ReSe Applications LLC, Wil, Switzerland) image rectification software for airborne optical scanner systems. Data from inertial measurement units installed on each sensor (IG-500N, SBG Systems S.A.S., Carrières-sur-Seine, France) were synchronised with each camera's imager and used as inputs for the software. Orthomosaicing thermal imagery was performed using Pix4D (version 3.1.23, Lausanne, Switzerland) photogrammetry software. Data pre-processing and image correction were as described in detail by Hernández-Clemente *et al.* (2012) and Zarco-Tejada *et al.* (2013).

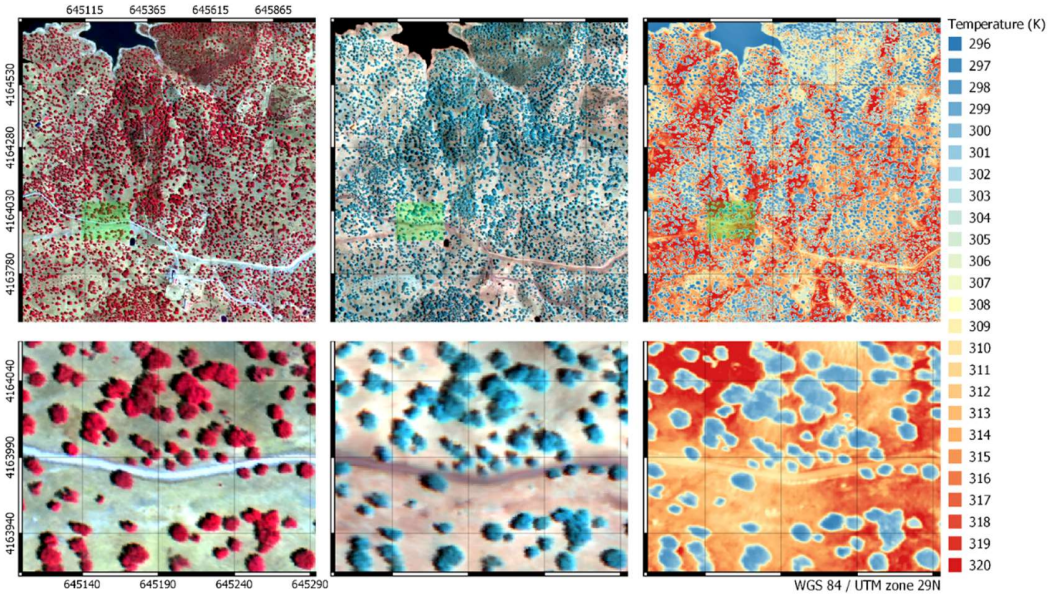

Figure 4. From left to right, the images from the VIS-NIR, NIR-SWIR, and thermal sensors are shown over the study area. Bottom row contains zoomed-in views of scenes above (green rectangle).

2.2.3 Spectral-based indicators

The high-resolution imagery acquired from each airborne sensor allowed us to identify and delineate tree crowns independently, seeking to minimise the effect of background and shadowing. This image segmentation was achieved using object-based methods through Niblack's threshold (Niblack, 1986) and Sauvola's binarisation techniques (Sauvola and Pietikäinen, 2000). Finally, we applied a binary watershed analysis using the Euclidean distance map for individual objects to automate the separation of the trees with overlapping crowns (Fig. 5).

Mean reflectance values for each tree were used to calculate 96 spectral-based indicators, including: i) VIs related to tree crown structure, chlorophyll, carotenoid, anthocyanin and water contents, and the epoxidation state of the xanthophyll cycle (detailed in Appendix A.); ii) chlorophyll fluorescence emission through the Fraunhofer line depth (FLD) method as described by Maier *et al.* (2003) using three bands for the in ($L_{763\ nm}$) and out ($L_{750\ nm}$; $L_{780\ nm}$) bands (3FLD); and iii) thermal dissipation using T_c-T_a, as previously described. We selected indicators mainly related to pigment composition and physiological variables to intensify the discriminatory capability of the models detecting healthy trees from trees with low severity levels (e.g. DS0 to DS1).

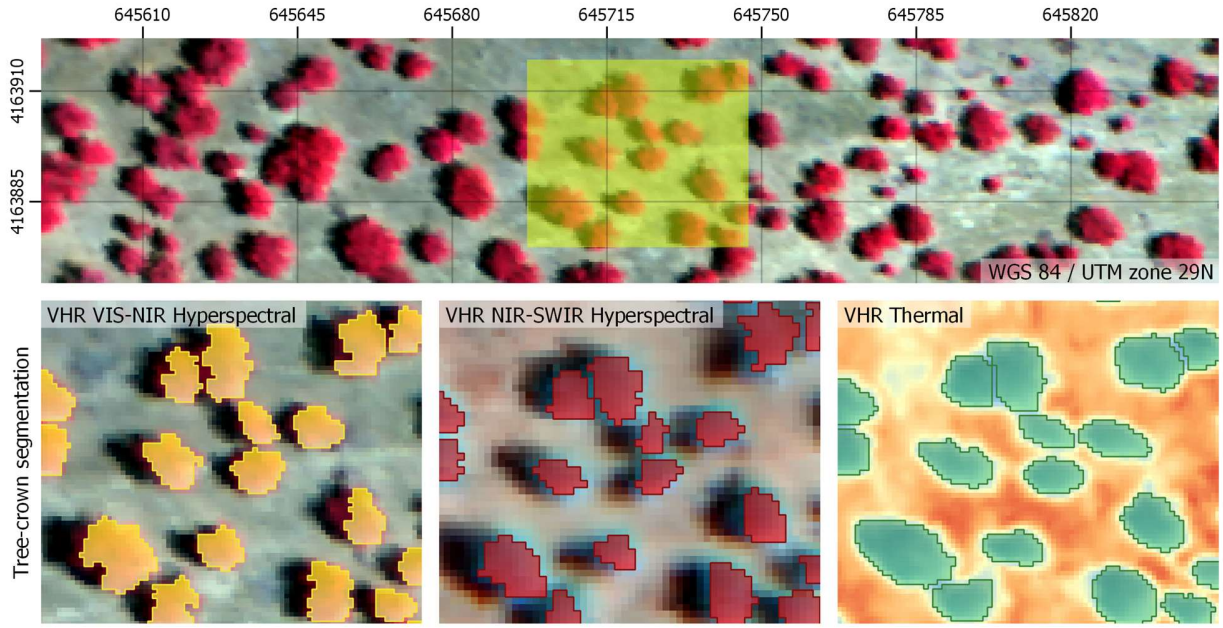

Figure 5. Overview of the entire crowns in the study area. Zoomed-in views (of the area in the yellow box) in the bottom row show the tree-crown segmentation for each sensor.

2.3. Model simulation analysis and plant trait retrieval

Canopy structural traits and biochemical composition were quantified by inverting the 3-D RTM FLIGHT8 model, using the pixels extracted from the tree crowns. We selected this model to minimise the impact of structural canopy variations, soil background, shadows and understory affecting the retrieval of PTs in heterogeneous forest canopies (Hernández-Clemente *et al.*, 2017; Hornero *et al.*, 2021). The model simulations were conducted using the atmospheric and ground data set collected during the image acquisition. Input variables for the model (Table 4) were established according to the

field measurements, estimates from existing literature, and nominal parameters to ensure that the generated look-up table (LUT) covered the range of spectral variability in the tree crowns. The ill-posed problem generated when a wide range of PTs can be obtained from the same spectrum was alleviated using restricting ranges of input parameters based on field data measurements (Combal *et al.*, 2003). The LUT calculation is processed in two phases, with the purpose of sequencing the inversion process to minimise the improperly posed problem and using the inversion methods best suited to each step, as detailed in Fig. 6. FLIGHT8 is coupled to leaf model FLUSPECT-B in the first phase to allow the retrieval of sun-induced fluorescence quantum efficiency (F_i) and with PROSPECT-D in the second phase to allow the retrieval of anthocyanins content.

Table 4
Inputs for the model simulation analysis.

Variable	Units	Acronym	Phase 1	Phase 2
Chlorophyll $a + b$ content	µg cm^{-2}	C_{ab}	10–60	21–33
Carotenoid content	µg cm^{-2}	C_{ar}	1–20	1–7
Water content	Cm	C_w	0.013	0–0.03
Dry matter content	g cm^{-2}	C_{dm}	0.024	0.003–0.018
Anthocyanin content	g cm^{-2}	A_{nth}	*NA**	0–6
Senescence material	Fraction	C_s	0	0
Mesophyll structure	–	N	2.1	2.1
Fluorescence quantum efficiency	–	F_i	0–0.2	*NA**
Leaf area index	m^2 m^{-2}	LAI	0–4	0.1–2.5
Leaf size	m	LFS	0.05	0.05
Leaf angle distribution	–	LAD	Spherical	Spherical
Fractional cover	%	FC	70	70
Soil reflectance	%	Soil	1 sample	1 sample
Understory reflectance	%	US	4 samples	4 samples
Crowns shape	–	CSh	Ellipsoid	Ellipsoid
Solar Zenith	deg.	SZA	25.84	25.84
Solar Azimuth	deg.	SAA	108.98	108.98

**NA*: F_i and A_{nth} are not modelled in PROSPECT-D and in Fluspect-B, respectively.

In the first phase of analysis (Fig. 6 top), we determined LAI, C_{ab}, C_{ar}, and the sun-induced fluorescence quantum efficiency (F_i). We built a LUT of +800k simulations coupling the FLUSPECT-B (Vilfan *et al.*, 2016) leaf reflectance model with the FLIGHT8 (Hornero *et al.*, 2021) canopy model. FLUSPECT-B considers the pigment concentrations in the leaf and its photosynthetic efficiency, and FLIGHT8 takes into account the structural properties of the canopy and the effect of the soil and the understory. The senescence material, water (C_w), and dry matter (C_{dm}) contents, and the structural parameter N were set to nominal values using a value previously determined on this particular species in the same study area following Hernández-Clemente *et al.* (2017) (Table 4 – Phase 1). For comparisons with airborne hyperspectral images, we used convoluted model simulations assuming Gaussian band spectral response functions for their corresponding FWHM, centred on the band locations of each imager. The LUT-based inversion followed a multi-step approach in which the LAI values were determined first, followed by C_{ab}, C_{ar}, and finally, F_i, using the MSR, $PSSR_b$, CRI_{700m}, and 3FLD spectral-based indicators as proxies for each PT, respectively.

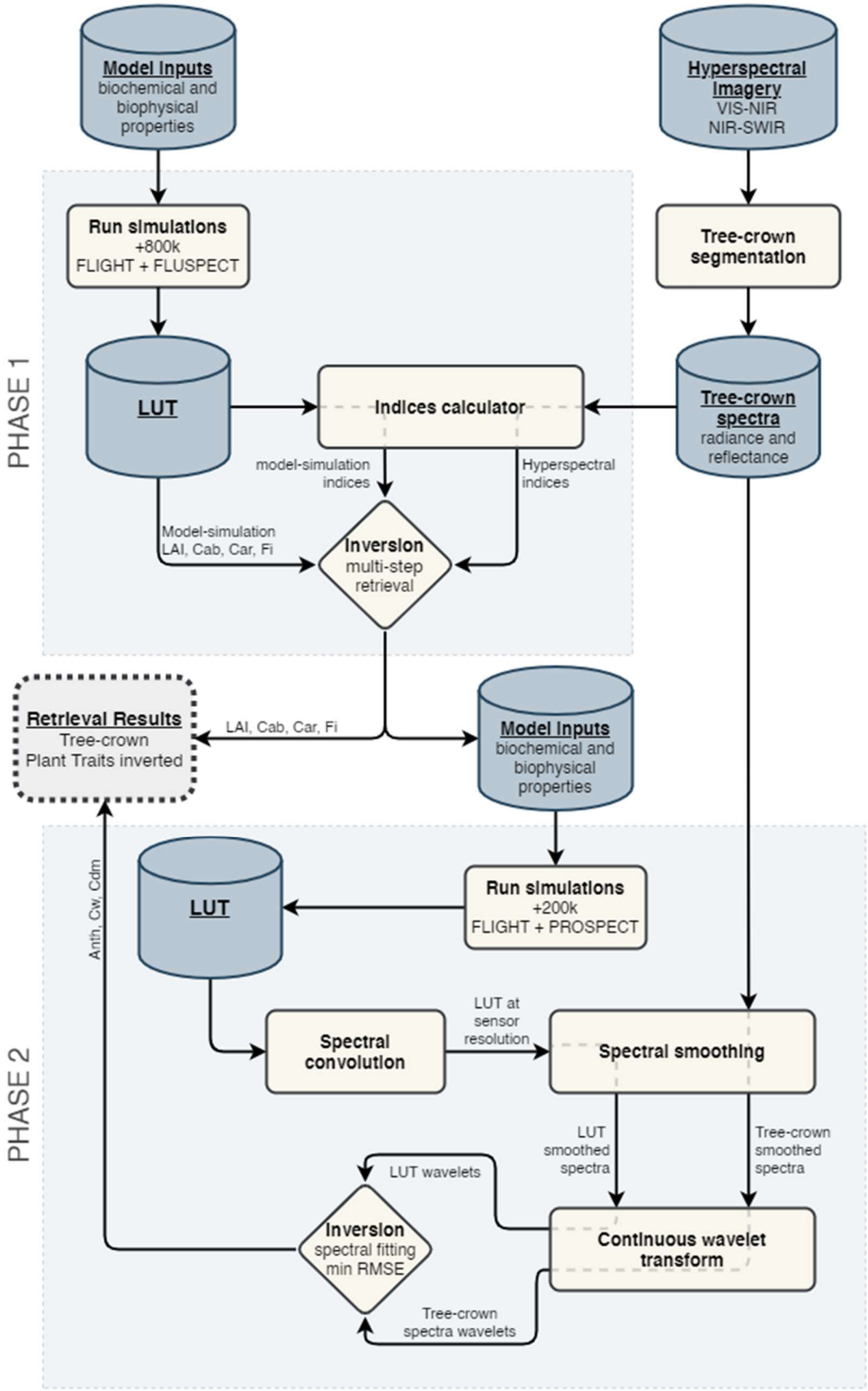

Figure 6. Model simulation approach diagram.

In the second phase, parameterisations retrieved from each tree were used to build a LUT of +200k simulations by coupling the PROSPECT-D (Féret *et al.*, 2017) leaf reflectance model with the FLIGHT8 canopy model. The leaf reflectance model was used to specifically quantify A_{nth}, as well as C_w and C_{dm} (Fig. 6 bottom). For the simulations and images, a smoothing algorithm based on local polynomial regression fitting (Cleveland *et al.*, 1992) was applied to eliminate the noise affecting the model inversion. Through the use of wavelets (Strang and Nguyen, 1996), we decomposed the hyperspectral signatures into frequency components at different spectral scales, allowing us to identify the LUT spectra that showed a closer correspondence to the image spectra, which enhances the retrieval of the spectral features and hence plant traits. The continuous wave transformation was performed over three spectral ranges, a) 470–710 nm, b) 670–850 nm, and c) 1000–1300 nm and 1500–1700 nm, for the retrieval of A_{nth}, C_{dm}, and C_w, respectively. At this stage, Kattenborn *et al.* (2017) and, more recently, Suarez *et al.* (2021) used a similar method to obtain the PTs from hyperspectral images; however, the methods used in this study differ in that a) an extended spectral range was used based on double-coupled hyperspectral imagers, and b) only the first four transformation scales were used to characterise more specific spectral regions of interest, instead of the whole range of the signal. The performance of the model-based PTs was evaluated based on the Normalised Root Mean Square Error (NRMSE) (2) with the field data (LAI, C_{ab}, C_{ar}, A_{nth}). F_s/F_i were excluded from this comparison since they are both unitless.

$$\text{NRMSE} = \sqrt{\frac{1}{n}\sum_{i=1}^{n}(y_i - \hat{y}_i)^2}\,\frac{1}{\bar{y}} \qquad (2)$$

where n is the number of observations, y_i represents the ith actual observation of the PT y, $\bar{y}$ its mean and $\hat{y}_i$ the predicted value from the model-based retrieval.

2.4. Plant trait selection and classification model approach

Once the PTs were obtained for each tree, feature selection was performed using a random forest (RF) classifier (Breiman, 2001; Liaw and Wiener, 2002) combined with an adaptation of an algorithm developed by Kursa and Rudnicki (2010), henceforth referred to as the Boruta algorithm. In the Boruta algorithm, shadow variables (permuted copies) are created by shuffling the original ones. The RF classifier is then applied to the initial data set, which is composed of the original variables and their shadow counterparts at the same time. The Boruta algorithm evaluates iteratively the importance of each original variable against the shadow variables to determine which variables are essential and at what magnitude. Variables are marked "Unconfirmed" when they are significantly lower than the shadows and are permanently discarded, while variables that are significantly higher than the shadows are marked "Confirmed". The process is repeated by re-generating the shadow variables and continues until only confirmed variables are left or until the maximum number of iterations defined at this stage is reached (set at 100 iterations). If the second scenario occurs, some variables may remain undecided, and they are considered "Tentative." The confidence level defined in the Boruta algorithm was established at 99% with a multiple comparisons adjustment using the Bonferroni method (Haynes, 2013) to control false positives. Once this process was completed, the importance of each PT in the severity and incidence classification process was obtained.

As an initial step, we performed the Boruta analysis using the field-based PT measurements, combining 2013, 2015, and 2017 evaluations, using only the three variables that were measured in all three years (F_s, C_{ab}, and C_{ar}) on 45 observations (15 evaluations and physiological measurements per year) and comparing them to the levels of severity and

incidence. The purpose of this analysis was to understand the sensitivity of field-based PT to forest decline.

The feature selection process started using all the model-based PTs retrieved for each tree, including 8 variables and 1146 observations. Then, the Boruta analysis was repeated for all the spectral-based indicators ($N = 96$). The objective was to improve the reliability of the model using complementary information added by VIs to the initial model-based PT feature selection. Due to the high fluctuations in the importance calculation when a large number of variables are used, the process in Boruta starts with three rounds, in which only the selected shadow variables are compared, while in the remaining rounds — up to 100 iterations — the original variables are compared with all the shadow variables. Figure 7a presents an overview of the entire process for the selection of variables conducted in this study.

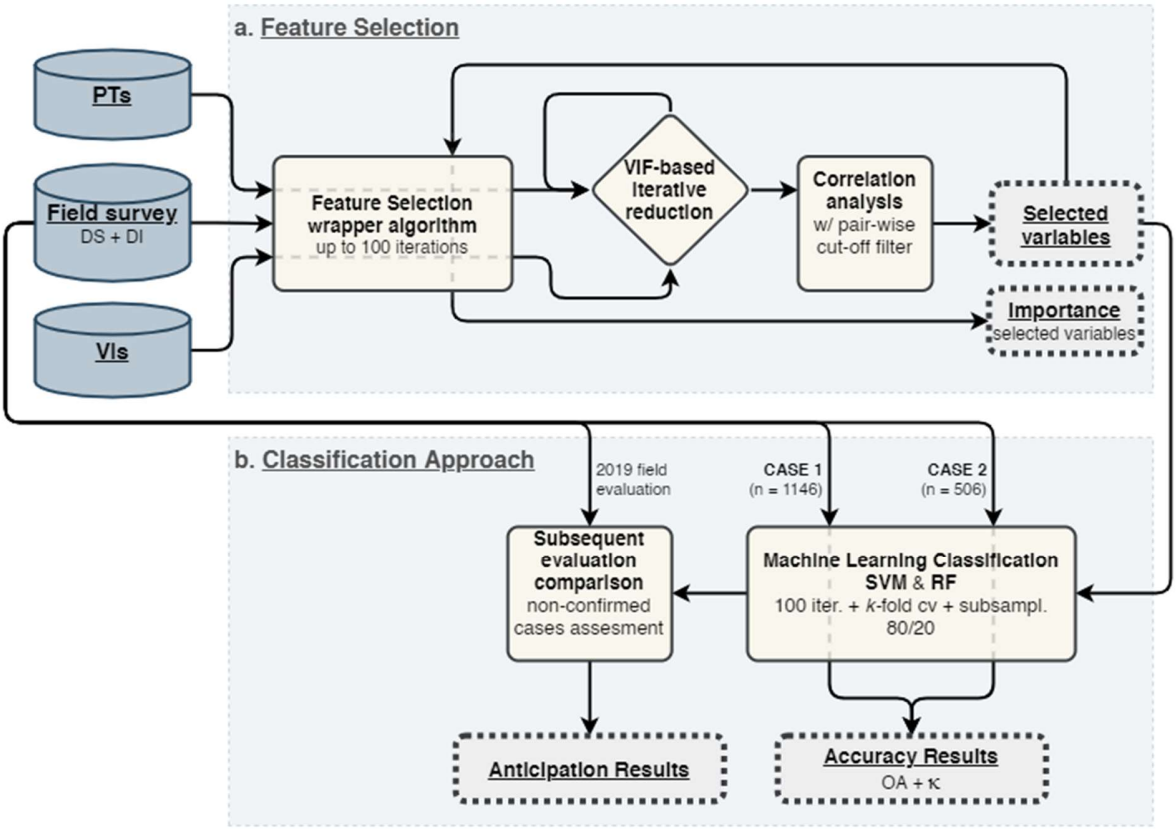

Figure 7. Overview of the methodology used for a) the feature selection using the Boruta algorithm, including the iterative reduction of variables and the correlation analysis; and b) the classification approach based on 2017 with the different cases assessed and a final comparison with a subsequent evaluation in 2019.

To strengthen the selection of features used in the classification model, the PTs were set in the established order according to their importance, and the VIs were added based on their previously calculated importance as well. At each stage of accumulation, the variance inflation factor (VIF) — an indicator that measures the extent to which the variance of an estimated regression coefficient increases due to collinearity (James *et al.*, 2013) — was calculated to avoid multicollinearity among the predictor variables. The variable was included only

if the VIFs for all variables were below the threshold of 10. The final set of selected variables (PTs + VI) was used in the next screening stage.

Finally, Pearson's correlation analysis and *p*-values were used to determine the degree of relationship between the previously selected variables. Through the calculated correlation matrix, the variables to be excluded were chosen to reduce the pair-wise correlations establishing a cutoff filter of 0.85 (Dormann *et al.*, 2013). The Boruta algorithm was applied to the remaining variables to determine the importance of each selected variable. A principal component analysis (PCA) was also conducted to determine to what extent the components capture the majority of the variance and to identify the variables that provide the most information and whether the less relevant ones could be discarded to reduce the dimensionality of the data set. The filtered variables were retained for the development of the classification model, as shown in Figure 7.

Two ML algorithms were used to classify disease incidence and severity levels: a supervised non-linear support vector machine (SVM) with a Gaussian kernel radial base function (Scholkopf *et al.*, 1997) and the RF algorithm (Breiman, 2001), which were reported as the predominant classifiers on airborne imaging (Gigović *et al.*, 2019; Gualtieri *et al.*, 1999; Liu *et al.*, 2017; Pal, 2005).

We evaluated models for two different cases (Fig. 7b), assessing incidence and severity classification from i) CASE 1, all trees assessed in 2017 ($N = 1146$), and ii) CASE 2, only confirmed trees, which were either still affected or unaffected again in 2019 ($N = 506$). To validate the selected models, we performed 100 iterations in which the data set was randomly divided into two samples, the training and the test samples by 80% and 20%, respectively, including *k*-fold cross-validation, in which the original sample was randomly partitioned into 10 equal-sized subsamples and repeated five times. Training data were subsampled for each iteration to avoid disproportionate frequencies of classes, which could negatively impact the model fit. Finally, we assessed the classification accuracy by calculating the overall accuracy (OA) and the Cohen's kappa coefficient (κ), which is based on comparing the observed agreement in a data set compared to what could occur by mere randomness (Richards and Jia, 1999).

After assessing the models' accuracy, we evaluated the anticipation capability using the visual evaluation 2 years later. In particular, we analysed whether the model was able to predict the unconfirmed cases — trees that were assessed at a given incidence level and in the subsequent assessment, 2 years later, were assessed at the opposing level — and refined towards those that improve or worsen, i.e., those that change from having incidence to not having it and the opposite, respectively. This last analysis helped us understand the applicability of the model to predict a subsequent evaluation of forest decline using the data from previous images and evaluations.

3. Results

In this section, we present the results of the evaluation of the field and PT indicators to predict oak decline. The predictions of the remote sensing spatial model are described below, focusing on the ability to discriminate between damage levels as a function of PT alterations caused by oak decline.

3.1. Plant trait indicator assessment based on forest health field measurements

The bi-annual empirical data collected from 2013 to 2017 show the capability of the field-based PTs — C_{ab}, C_{ar}, and F_s — to discriminate different levels of severity. Trees with low disease severity levels consistently had high values for F_s, C_{ab}, and C_{ar} content (Fig. 8). F_s was identified as having importance values two times higher than C_{ab} and C_{ar} in both severity and incidence levels (Fig. 8 right side).

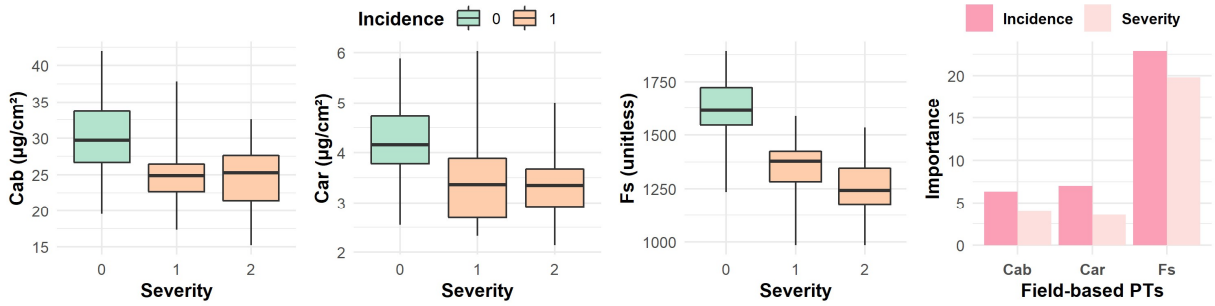

Figure 8. Relationship between the level of severity and field-based plant traits – chlorophyll content (C_{ab}), carotenoid content (C_{ar}), and steady-state leaf fluorescence (F_s) – in $N = 45$ trees measured in 2013, 2015, and 2017. Importance scores for field-based plant traits in detecting oak decline computed via the Boruta algorithm are shown at right.

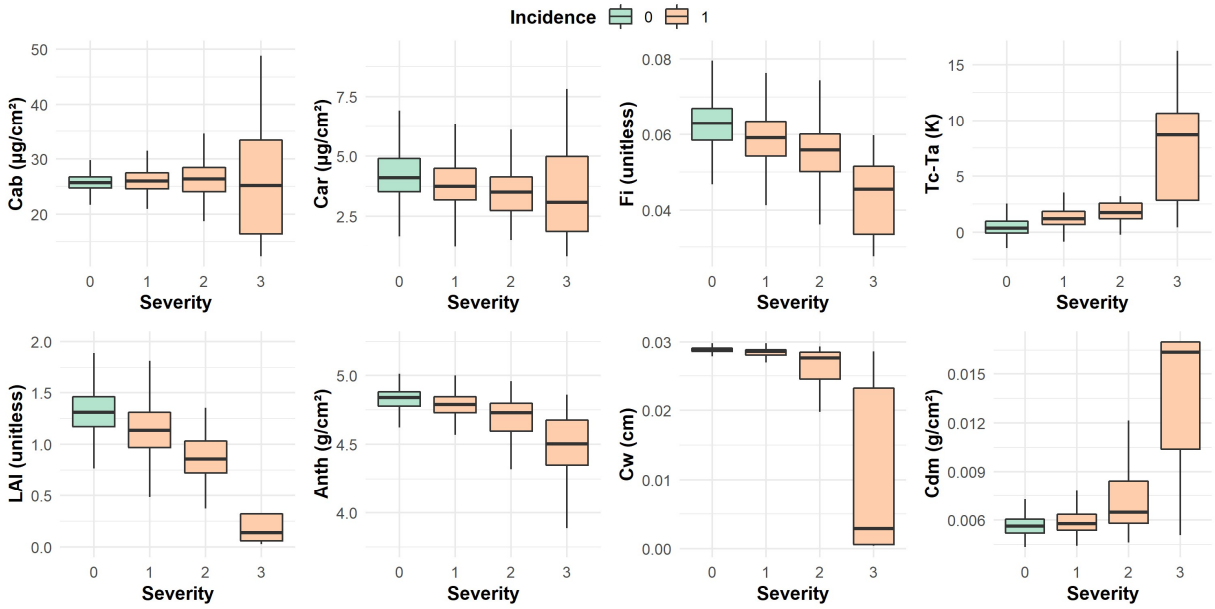

Figure 9. Relationship between severity and plant traits retrieved from hyperspectral and thermal images in 2017.

3.2. Spectral- and model-based plant trait predictors of oak decline

As with empirical measurements, model-based values of F_i and pigment content (C_{ab} and C_{ar}) were inversely related to severity level (Fig. 9). The model-based PTs corresponded well with field data, having relatively low normalised error ($NRMSE_{LAI}$ = 0.13, $NRMSE_{Cab}$ = 0.16, $NRMSE_{Car}$ = 0.2, and $NRMSE_{Anth}$ = 0.12) and values within the expected range (data not shown). In Fig. 9, we also included the model-based retrievals of three other PTs (C_w, C_{dm}, and A_{nth}) and T_c-T_a derived from thermal data. Severity level was positively associated with T_c-T_a and C_{dm} but negatively associated with LAI, A_{nth}, and C_w. These results are also consistent with the classification of incidence and severity obtained from field-based PT measurements, described in the previous section, where F_s was one of the most relevant variables to detect oak decline.

Variable importance scores for model-based PTs and T_c-T_a are presented in Fig. 10. T_c-T_a and F_i had the highest importance scores in models

discriminating the first and second severity levels, while LAI and C_{dm} were determined to be the most important for differentiating the remaining severity levels (Fig. 11a).

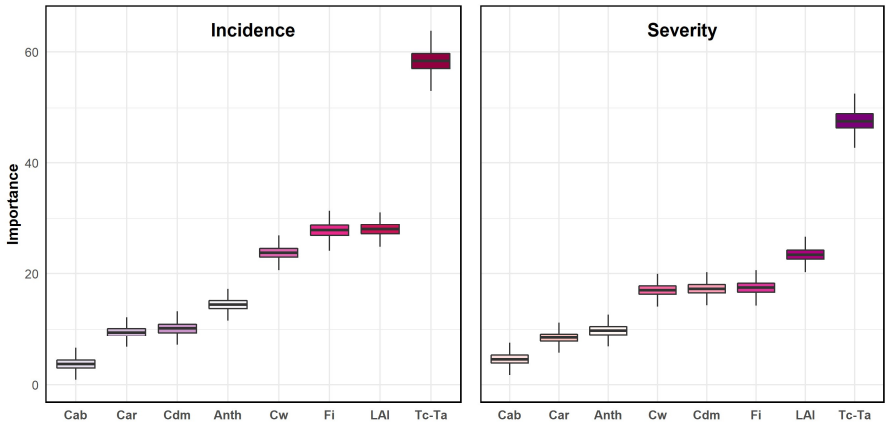

Figure 10. Overall importance scores for each plant trait when classifying both incidence and severity disease levels using the Boruta algorithm.

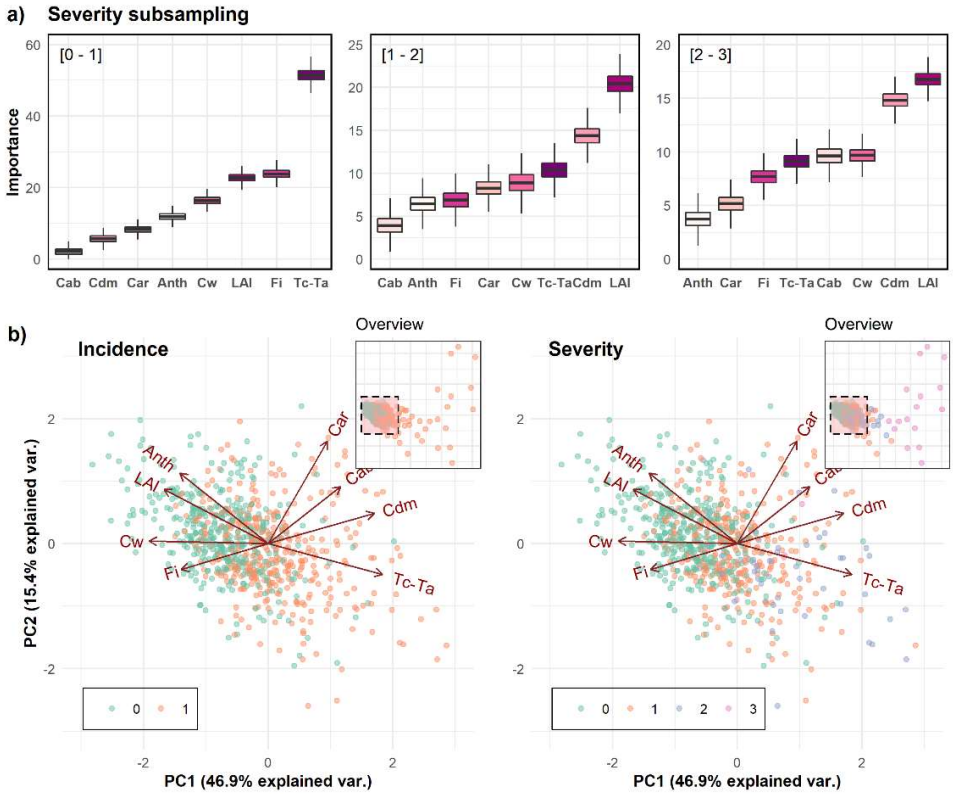

Figure 11. Severity subsampling importance scores for each plant trait (PT) (a) and spectral-based principal component (PC) predictors' analysis (b) for both incidence (0–1) and severity (0–3) levels using the model-based PTs (C_{ab}, C_{ar}, A_{nth}, C_w, C_{dm}, LAI, and F_i) and the thermal-image-based PT (T_c-T_a). The bidimensional plots display each variable's loading, with vectors and the tree samples as points coloured by

severity and incidence levels. The vectors' length approximates the variance represented by each variable, whereas the angles between them represent their correlations.

The principal components PC1 and PC2 explain 59.2% of the total variability, with 42.5% for PC1 and 16.7% for PC2 (Fig. 11b). The PTs T_c-T_a and LAI were strongly negatively correlated in PC1 and PC2 space, having nearly the same magnitude and angle but different directions. These results may indicate that the more abundant the vegetation, the greater the transpiration capacity and the lower the temperature difference. On an orthogonal ray, we find C_{ar}, which is scarcely related to them, and its importance indicates its limited contribution to the model. The projection of F_i in the first two components was opposite that of C_{ar}, and this variable contributed substantially to model performance. This variable was more important than LAI for the development of an incidence classification model as well as distinguishing the first two severity levels.

3.3. Remote sensing spatial model predictions of oak decline

To find the best variables for predicting oak decline, the model-based PTs were combined with 95 VIs, of which only four passed the iterative VIF screening and pair-wise correlation threshold: LIC_3, CI_2, GnyLi, and MND (Fig. 12a). The variables with the lowest correlation coefficient (<0.05) were C_{ar} with LAI, A_{nth}, and MND, a result that is consistent with the PCA showing C_{ar} as largely independent from other variables.

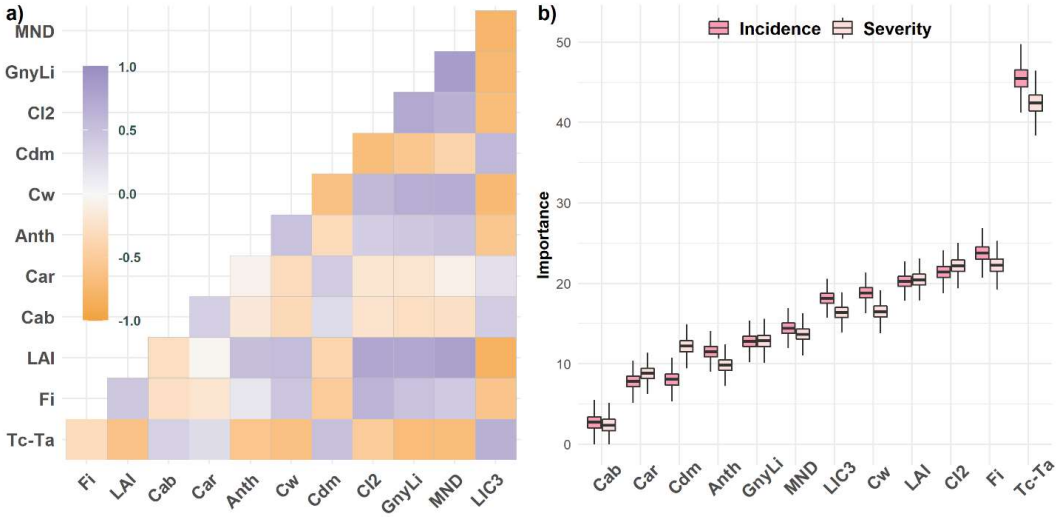

Figure 12. Plant traits (PTs) and vegetation indices (VIs) correlations (a) and variable importance scores for spectral-based PT and VIs with severity and incidence (b) to detect oak decline.

The variable selection process yielded 12 final indicators with a VIF below the established threshold. Two indicators were associated with photosynthesis regulation: F_i and T_c-T_a. Four indicators were related to pigment content: C_{ab}, C_{ar}, A_{nth}, and CI_2. One indicator was related to fractional cover, namely, LAI. Five indicators were related to water content: C_w, C_{dm}, GnyLi, MND, and LIC_3. Among all the indicators, the variables contributing the most to detecting different levels of incidence and severity were T_c-T_a and F_i. These PTs were included as predictors for the final

classification model of oak decline; their importance scores are presented in Figure 12b. Variables with the highest importance included T_c-T_a, F_i, and CI_2.

Model accuracy was estimated on the basis of the total number of trees evaluated and confirmed cases reported in the subsequent survey (Fig. 13). Models classifying severity had an overall accuracy of 0.71 ($\kappa = 0.51$) in the best case (sampling of confirmed cases with RF algorithm). Models classifying incidence were more accurate (OA = 0.82; $\kappa = 0.62$) for this same scenario. The SVM algorithm was slightly more accurate when we used the complete data set (all trees; $N = 1146$), while RF performed better with the reduced-input data set (confirmed cases; $N = 506$). For models predicting incidence, the OAs were greater than 0.75 (thus considered 'high'), and the Cohen's kappa scores were fair to excellent, according to Cicchetti and Sparrow (1981).

The findings obtained when evaluating the anticipation capabilities (Table 5) indicate a better behaviour of the RF algorithm when building the model with both confirmed cases — in which the best result is found — and all cases. When we analyse the prediction rate while segregating between trees that worsen (incidence: $0 \rightarrow 1$) and those that improve ($1 \rightarrow 0$), for the former, the RF algorithm behaves better, and for the latter, SVM.

Example predictions from a final incidence classification model using the SVM algorithm are presented in Fig. 14, with results within the expected performance (OA = 0.81; $\kappa = 0.62$); comprehensive statistics are detailed in Appendix B. Through this map and the field evaluations, the differences found can be appreciated, as well as their spatial variability.

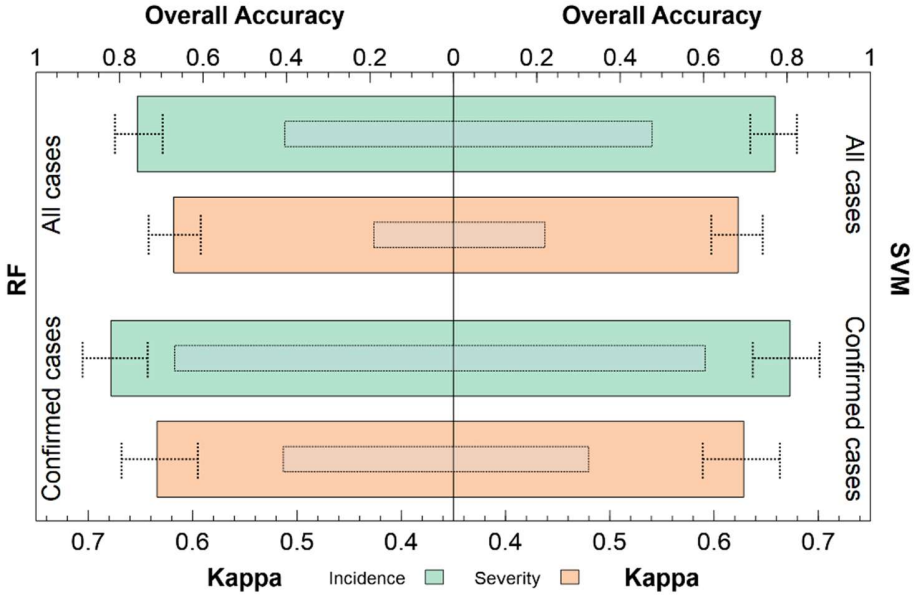

Figure 13. Overall accuracy (OA) and Cohen's kappa scores for classification models. Results were obtained from 100 iterations of random data subsets for training and validation (80/20). Average OA and kappa values are shown as horizontal bars, the former in colour and the latter as narrower grey bars with dotted edges. The error bars indicate the minimum and maximum OA values across iterations.

Table 5

Prediction rate for non-confirmed cases (NC) using models built with all cases or only confirmed ones. The best results for each case are highlighted in light green and in darker green overall.

Method	Sample	NC $_{0\leftrightarrow1}$ (%)	NC $_{0\rightarrow1}$ (%)	NC $_{0\leftarrow1}$ (%)
SVM	All cases	29.9	27.4	34.0
SVM	Confirmed cases	33.8	34.8	32.1
RF	All cases	32.1	31.9	32.0
RF	Confirmed cases	35.5	40.2	27.4

All cases: $N = 1146$; confirmed cases: $N = 506$.

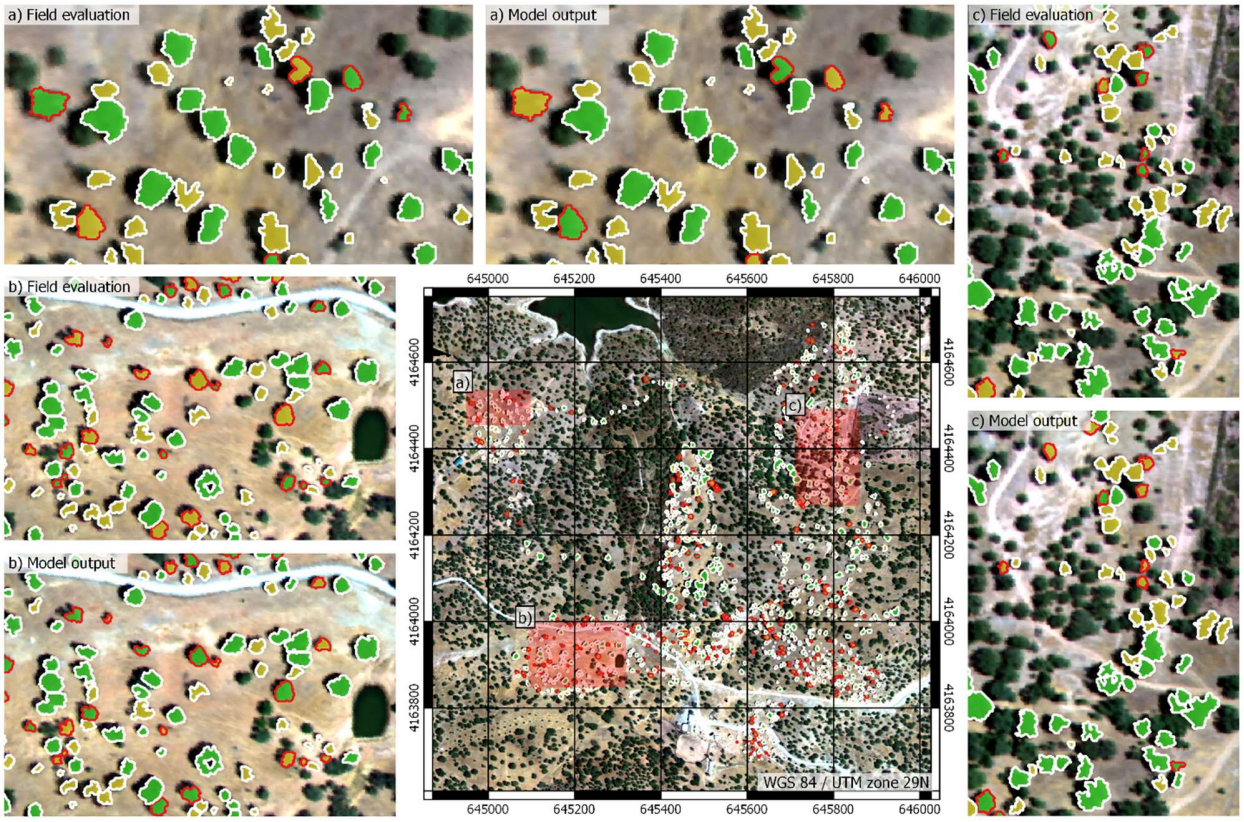

Figure 14. Field evaluation and spatial prediction map from the model output. Yellow and green filling indicates incidence or not, respectively. Tree crowns with a red outline are those that differ between the field evaluation and the model output.

4. Discussion

The first objective of this study was to identify the PTs that are most useful for detecting the incidence and severity of decline symptoms in holm oak. One of the main challenges encountered in quantifying PTs in heterogeneous forest canopies was to minimise the impacts of shadows, soil background, and understory, which dilute the spectral signature of pure crowns (Hernández-Clemente *et al.*, 2019; Liu *et al.*, 2020; Markiet *et al.*, 2016; Pisek *et al.*, 2015). For this reason, advanced 3-D simulation models designed specifically for heterogeneous forest canopies were a major methodological component of this study. The critical step resided in the successful retrieval of model-based PTs that allowed us to understand the contribution to each PT and complete the ML modelling approach with additional information derived from other spectral-based, uncorrelated variables.

Field data confirmed the association between *Q. ilex* status and several key PTs. Trees with lower disease incidence had higher values of C_{ab}, C_{ar}, and F_s. As symptom severity increases, the concentration of these pigments and the chlorophyll fluorescence decrease. The decrease rate we observed in chlorophyll fluorescence and pigment content associated with disease incidence are consistent with declines associated with drought and root rot stress found in other experiments under controlled conditions (Früchtenicht *et al.*, 2018; Koller *et al.*, 2013; Ruiz Gómez *et al.*, 2018) and field surveys (Baquedano and Castillo, 2007; Camarero *et al.*, 2012).

It is notable that we found F_s to be more important than the other two PTs in identifying disease incidence from field data. Among model-based PTs retrieved from hyperspectral images, F_i similarly had a higher importance score than any other pigment content indicator for discriminating severity. This pattern is consistent with the variable importance ranking of variables in Zarco-Tejada *et al.* (2018) for detecting *Xf*-induced symptoms in olive trees.

Including spectral-based PT indicators in our analysis provided insight into the functional responses of oak trees to different disease levels. T_c-T_a was the most important indicator, regardless of whether we discriminate by incidence or severity. Thermal imaging has improved the detection of several crop diseases in other studies, including *Verticillium* wilt in olive orchards (Calderón *et al.*, 2015), water stress in peach orchards (Gonzalez-Dugo *et al.*, 2020), and red leaf blotch in almond orchards (López-López *et al.*, 2016). In this study, other important PTs included LAI and F_i, followed by C_{dm}, C_w, and A_{nth}, and to a lesser extent C_{ab} and C_{ar}.

Focusing on the discrimination capacity of each PT between the different stages of severity, T_c-T_a was generally an important predictive variable for determining disease incidence, but LAI and C_{dm} were more relevant for discriminating mild and advanced severity classes. PCA showed that T_c-T_a and LAI contributed strongly to the same component but in opposite directions. Severity subsampling supports that while canopy temperature is particularly important for early incidence detection, LAI may provide more information about severity levels when a tree is infected.

Another important aspect of this study is the consideration of VIs alongside other model-based PTs for classification. CI_2, GnyLi, MND, and LIC_3 were variables that passed through selection criteria, providing additional information and avoiding collinearity with other variables. In the final model, F_s was selected as highly important, since part of the weight of LAI was distributed among other indicators such as CI_2 or LIC_3. The importance of indicators from the SWIR region (MND and GnyLi) also exceeded that of C_{ab}, C_{ar}, C_{dm}, and A_{nth}.

This study showed that remotely derived PTs can support the early detection of holm oak decline, which was the second objective of this work. By applying a combination of 3-D model simulation and statistical analysis using ML approaches, we found that oak forest decline can potentially be detected at an earlier stage and that severity levels can be accurately assessed at broad scales. Predictive model accuracy was high, with an OA $>$ 0.8 and $\kappa > 0.6$, indicating that the PTs we identified may be helpful for understanding physiological responses to disease and other stressors. The model accuracy achieved in this study is comparable to that of prediction models developed for olive trees by Zarco-Tejada *et al.* (2018). Taking advantage of a subsequent field evaluation performed 2 years later, the model's anticipation ability was evaluated, which brought us significantly improved results since it managed to anticipate up to 40% in the best scenario.

These results help bridge a gap in the understanding of how forest decline alters PTs via complex interactions between biotic and abiotic factors. Unlike in agricultural studies, where factors such as nutrient deficiency or water availability can be controlled, in forests these interactions are difficult to dissociate. Forest canopy heterogeneity poses a challenge for spectral data modelling, due to discontinuous architectures and interference from shadows, understory, and soil composition. The utility of satellite-based spectral indicators for detecting diseases has been examined by Hornero *et al.* (2020) in olive trees and Hernández-Clemente *et al.* (2017) in holm oak. A common finding in these studies was that the soil and the understory both influence the spectral signature and the fluorescence signal of aggregated pixels. In this work, we used the FLIGHT8 model, a recently improved version of the FLIGHT model, which minimises background effects by considering the spectral contribution of the understory. The success of the methods presented here may be partially due to the high spatial resolution of hyperspectral images collected and to the open nature of the woodland landscape. However, the FLIGHT8 model also accounts for increasing levels of pixel aggregation (e.g., using medium- to low-resolution satellite imagery) in heterogeneous canopies (Hornero *et al.*, 2021). Future work should investigate the assessment and validation of the methods presented here performed with satellite imagery and/or different types of forest canopies.

In a practical level for the management of holm oak decline, the results show that T_c-T_a, F_i, LAI and C_{dm} are sensitive indicators to discriminate between DI levels [0–1]. However, being able to quantify between DS [0–4] is clearly advantageous for effective management and mitigation of forest decline. According to the results, monitoring holm oak decline should include the analysis of the transition between severity levels based on indicators such as T_c-T_a, F_i and LAI to discriminate between DS [0–1]; LAI, C_{dm}, and T_c-T_a between DS [1–2]; and LAI, C_{dm} and C_w between DS [2–3]. The transition between DS [0–1] is particularly important, as it indicates the progression between non-symptomatic to symptomatic trees.

The proposed methodology has been validated on holm oak decline affected jointly by the presence of *Pc* and abiotic stress, mainly water stress. But the methods proposed here should be further tested to analyse the sensitivity of PTs to disentangle the interactive biotic and abiotic effects. Future studies should thus include the analysis of a wider range of holm oak forest locations solely affected by either abiotic or abiotic factors. This situation is quite unlikely, as it has been shown that holm oak decline is often linked to a combination of factors (Camilo-Alves *et al.*, 2013; Corcobado *et al.*, 2014). However, each factor may have different contribution in the decline process (Colangelo *et al.*, 2018). Therefore, the discrimination between both factors should be considered in future studies. Furthermore, the sensitivity of PTs in oak forest affected by other types of pathogens or abiotic stress could be different. This work provides a

breakthrough in analysing the spectral changes caused by xylem-limited factors such as root rot, water stress or soil compaction in heterogeneous forest stands. The challenge is to evaluate other types of forest decline processes on the methodological and empirical basis shown in this work.

Large-scale monitoring may be further improved by including multitemporal data to track disease evolution. However, such data will increase the complexity of analyses, particularly due to variation in understory and soil reflectance from image to image, their impact on aggregated pixels, and the need to account for those variations with RTM. The methodology presented here may be particularly relevant for the Sentinel-2 mission, which provides multitemporal data in the visible, infrared, and short infrared regions, and the FLEX mission, which will provide fluorescence data after 2022.

5. Conclusions

This study develops a new methodology that integrates field data, airborne imagery, physical RTM, and empirical modelling to retrieve PTs and assess their association with forest decline and provides a tool to detect early-onset symptoms of decline in holm oak. Hyperspectral image data, including VNIR and SWIR spectral regions, combined with thermal imaging and RTM can be used to monitor the spread of forest decline over large areas. Thermal-based canopy temperature (T_c-T_a) was the most important PT in the model to discriminate between different levels of severity and incidence, followed by the fluorescence (F_i) and LAI, whereas LAI and C_{dm} were the most relevant indicators for discriminating advanced stages of severity. Additional spectral indicators such as CI_2 or LIC_3 complemented LAI, and VIs in the SWIR region (GnyLi and MND) were more important than PTs such as C_{ab}, C_{ar}, or A_{nth}. Overall, our results demonstrate that an integrated approach combining spectral- and model-based PT retrievals using 3-D RTM and classification methods is needed for the large-scale monitoring of forest decline. This approach enabled the successful prediction of holm oak decline at an early stage; it is essential to monitor harmful forest diseases, and this task can be augmented through the retrieval of accurate forest health traits from advanced airborne imagery and satellite data observations.

Acknowledgements

Data collection was partially supported by the QUERCUSAT (CGL2013-40790-R) and ESPECTRAMED (CGL2018-86161-R) projects, part of the Spanish Research Agency, Ministry of Science and Innovation. A. Hornero was supported by research fellowship DTC GEO 29 “Detection of global photosynthesis and forest health from space” from the Science Doctoral Training Centre (Swansea University, United Kingdom). P. North was supported by the NERC National Centre for Earth Observation (United Kingdom). F.J. Ruiz-Gómez was supported by a post-doctoral fellowship of the Junta de Andalucía (Spain) and the European Social Fund 2014-2020 Program (DOC_0055). The authors would also like to thank QuantaLab-IAS-CSIC (Spain) for laboratory assistance and the support provided during the airborne campaigns and image processing. A. Walter, F.J. Romero-Ramirez, J.M. Higuera, and R. Cabrera are acknowledged for their support during the field campaigns.

All the figures included in this manuscript were designed taking into account colour schemes prepared for people with visual disabilities and ensuring that they can be printed correctly (Harrower and Brewer, 2003).

Appendix A.

Vegetation indices derived from airborne imagery included in this study and their formulations.

Vegetation index	Equation	Reference
Structural		
Normalized Difference Vegetation Index	$NDVI = (R_{800} - R_{670})/(R_{800} + R_{670})$	(Rouse *et al.*, 1974)
Near-Infrared Reflectance of Vegetation	$NIR_V = R_{800}(R_{800} - R_{670})/(R_{800} + R_{670})$	(Badgley *et al.*, 2017)
Renormalized Difference Vegetation Index	$RDVI = (R_{800} - R_{670})/\sqrt{(R_{800} + R_{670})}$	(Roujean and Breon, 1995)
Simple Ratio	$SR = R_{800}/R_{670}$	(Jordan, 1969)
Modified Simple Ratio	$MSR = (R_{800}/R_{670} - 1)/(\ \mathbb{I}(R_{800}/R\_670)\mathbb{I}\ \text{^}0.5 + 1)$	(Chen, 1996)
Optimized Soil-Adjusted Vegetation Index	$OSAVI = (1 + 0.16)\ \frac{R_{800} - R_{670}}{R_{800} + R_{670} + 0.16}$	(Rondeaux *et al.*, 1996)
Modified Soil-Adjusted Vegetation Index	$MSAVI =\ (1 + L)\frac{R_{800} - R_{670}}{R_{800} + R_{670} + L}$	(Qi *et al.*, 1994)
Modified Triangular Vegetation Index 1	$MTVI_1 = 1.2(1.2(R_{800} - R_{550}) - 2.5(R_{670} - R_{550}))$	(Haboudane *et al.*, 2004)
Modified Triangular Vegetation Index 1	$MTVI_2 = 1.5\frac{1.2(R_{800} - R_{550}) - 2.5(R_{670} - R_{550})}{\sqrt{(2R_{800} + 1)^2 - \left(6R_{800} - 5\sqrt{R_{670}}\right) - 0.5}}$	(Haboudane *et al.*, 2004)
Modified Chlorophyll Absorption Ratio Index	$MCARI = ((R_{700} - R_{670}) - 0.2(R_{700} - R_{550}))\left(\frac{R_{700}}{R_{670}}\right)$	(Haboudane *et al.*, 2002)
Modified Chlorophyll Absorption Ratio Index 1	$MCARI_1 = 1.2(2.5(R_{800} - R_{670}) - 1.3(R_{800} - R_{550}))$	(Haboudane *et al.*, 2004)
Modified Chlorophyll Absorption Ratio Index 2	$MCARI_2 = 1.5\frac{2.5(R_{800} - R_{550}) - 1.3(R_{670} - R_{550})}{\sqrt{(2R_{800} + 1)^2 - \left(6R_{800} - 5\sqrt{R_{670}}\right) - 0.5}}$	(Haboudane *et al.*, 2004)
Enhanced Vegetation Index	$EVI = 2.5(R_{800} - R_{670})/(R_{800} + 6R_{670} - 7.5R_{400} + 1)$	(Huete *et al.*, 2002)
Lichtenthaler 1	$LIC_1 = (R_{800} - R_{680})/(R_{800} + R_{680})$	(Lichtenthaler, 1996)
Pigments		
Vogelmann 1	$VOG_1 = R_{740}/R_{720}$	(Vogelmann, 1993)
Vogelmann 2	$VOG_2 = (R_{734} - R_{747})/(R_{715} + R_{726})$	(Vogelmann, 1993)
Vogelmann 3	$VOG_3 = (R_{734} - R_{747})/(R_{715} + R_{720})$	(Vogelmann, 1993)
Gitelson and Merzlyak 1	$GM_1 = R_{750}/R_{550}$	(Gitelson and Merzlyak, 1996)
Gitelson and Merzlyak 2	$GM_2 = R_{750}/R_{700}$	(Gitelson and Merzlyak, 1996)
Transformed Chlorophyll Absorption Ratio	$TCARI = 3\left(\begin{matrix}(R_{700} - R_{670}) - \\ -0.2\ (R_{700} - R_{550})\frac{R_{700}}{R_{670}}\end{matrix}\right)$	(Haboudane *et al.*, 2002)
TCARI/OSAVI	$TCARI/OSAVI = \frac{\mathrm{TCARI}}{\mathrm{OSAVI}}$	(Haboudane *et al.*, 2002)
Chlorophyll Index	$CI = \frac{R_{750}}{R_{710}}$	(Zarco-Tejada *et al.*, 2001)
Triangular Vegetation Index	$TVI = 0.5(120(R_{750} - R_{550}) - 200(R_{670} - R_{550}))$	(Broge and Leblanc, 2001)
Simple Ratio Pigment Index	$SRPI = R_{430}/R_{680}$	(Penuelas *et al.*, 1995)
Normalized Phaeophytinization Index	$NPQI = (R_{415} - R_{435})/(R_{415} + R_{435})$	(Barnes *et al.*, 1992)
Normalized Pigment Chlorophyll Index	$NPCI = (R_{680} - R_{430})/(R_{680} + R_{430})$	(Penuelas *et al.*, 1995)
Simple Ratio 695/420 Carter	$CTR = R_{695}/R_{420}$	(Carter, 1994)
Simple Ratio Carotenoids	$CAR = R_{515}/R_{570}$	(Hernández-Clemente *et al.*, 2012)

Datt Cab Cx+c Index	$DCabxc = R_{672}/ (3\ R_{550}R_{708})$	(Datt, 1998)
Datt NIR Cab Cx+c Index	$DNCabxc = R_{860}\ /\ (R_{550}R_{708})$	(Datt, 1998)
Structure Insensitive Pigment Index	$SIPI = (R_{800} - R_{445})/(R_{800} + R_{680})$	(Penuelas *et al.*, 1995)
Carotenoid Reflectance Index 550	$CRI_{550} = 1/R_{510} - 1/R_{550}$	(Gitelson *et al.*, 2006, 2003)
Carotenoid Reflectance Index 700	$CRI_{700} = 1/R_{510} - 1/R_{700}$	(Gitelson *et al.*, 2006, 2003)
Modified Carotenoid Reflectance Index 550	$CRI_{550m} = 1/R_{515} - 1/R_{550}$	(Gitelson *et al.*, 2006, 2003)
Modified Carotenoid Reflectance Index 700	$CRI_{700m} = 1/R_{515} - 1/R_{700}$	(Gitelson *et al.*, 2006, 2003)
Near-Infrared Carotenoid Reflectance Index 550	$RCRI_{550} = 1/R_{510} - (1/R_{550})\ R_{770}$	(Gitelson *et al.*, 2006, 2003)
Near-Infrared Carotenoid Reflectance Index 700	$RCRI_{700} = 1/R_{510} - (1/R_{700})\ \ R_{770}$	(Gitelson *et al.*, 2006, 2003)
Plant Senescence Reflectance Index	$PSRI = (R_{680} - R_{500})/R_{750}$	(Merzlyak *et al.*, 1999)
Lichtenthaler 3	$LIC_3 = R_{440}/R_{740}$	(Lichtenthaler, 1996)
PRIs		
Photochemical Reflectance Index	$PRI = (R_{570} - R_{531})/(R_{570} + R_{531})$	(Gamon *et al.*, 1992)
Photochemical Reflectance Index 515	$PRI_{515} = (R_{515} - R_{531})/(R_{515} + R_{531})$	(Hernández-Clemente *et al.*, 2011)
Modified Photochemical Reflectance Index 1	$PRIM_1 = (R_{512} - R_{531})/(R_{512} + R_{531})$	(Gamon *et al.*, 1992)
Modified Photochemical Reflectance Index 2	$PRIM_2 = (R_{600} - R_{531})/(R_{600} + R_{531})$	(Gamon *et al.*, 1992)
Modified Photochemical Reflectance Index 3	$PRIM_3 = (R_{670} - R_{531})/(R_{670} + R_{531})$	(Gamon *et al.*, 1992)
Modified Photochemical Reflectance Index 4	$PRIM_4 = (R_{570} - R_{531} - R_{670})/(R_{570} + R_{531} + R_{670})$	(Gamon *et al.*, 1992)
Normalized PRI	$PRIn = PRI/(RDVI\ R_{700}/R_{670})$	(Zarco-Tejada *et al.*, 2013)
PRI×CI	$PRI \times CI = PRI(R_{760}/R_{700} - 1)$	(Garrity *et al.*, 2011)
BGR		
Blueness Index	$B = R_{450}/R_{490}$	-
Greenness Index	$G = R_{550}/R_{670}$	(Zarco-Tejada *et al.*, 2001)
Redness index	$R = R_{700}/R_{670}$	(Gitelson *et al.*, 2000)
Blue/Green Index 1	$BGI_1 = R_{400}/R_{550}$	(Zarco-Tejada *et al.*, 2012, 2005)
Blue/Green Index 2	$BGI_1 = R_{450}/R_{550}$	(Zarco-Tejada *et al.*, 2012, 2005)
Blue Fraction 1	$BF_1 = R_{400}/R_{410}$	-
Blue Fraction 2	$BF_2 = R_{400}/R_{420}$	-
Blue Fraction 3	$BF_3 = R_{400}/R_{430}$	-
Blue Fraction 4	$BF_4 = R_{400}/R_{440}$	-
Blue Fraction 5	$BF_5 = R_{400}/R_{450}$	-
Blue/Red Index 1	$BRI_1 = R_{490}/R_{690}$	(Zarco-Tejada *et al.*, 2012)
Blue/Red Index 2	$BRI_2 = R_{450}/R_{690}$	(Zarco-Tejada *et al.*, 2012)
Relative Greenness Index	$RGI = R_{690}/R_{550}$	(Ceccato *et al.*, 2001)
Ratio Analysis of Reflectance Spectra	$RARS =\ R_{746}/R_{513}$	(Chappelle *et al.*, 1992)
Lichtenthaler 2	$LIC_2 = R_{440}/R_{690}$	(Lichtenthaler, 1996)
Healthy Index	$HI = (R_{534} - R_{698})/(R_{534} + R_{698}) -\ R_{704}/2$	(Mahlein *et al.*, 2013)

Curvature Optical Index	$CUR = (R_{675}\ R_{690})/(R_{683})^2$	(Zarco-Tejada *et al.*, 2000)
NIR-VIS		
Pigment Specific Simple Ratio A	$PSSR_a = R_{800}/R_{680}$	(Blackburn, 1998)
Pigment Specific Simple Ratio B	$PSSR_b = R_{800}/R_{635}$	(Blackburn, 1998)
Pigment Specific Simple Ratio C	$PSSR_c = R_{800}/R_{470}$	(Blackburn, 1998)
Pigment Specific Normalised Difference C	$PSND_c = (R_{800} - R_{470})/(R_{800} + R_{470})$	(Blackburn, 1998)
Anthocyanins		
Visible Atmospherically Resistant Index	$VARI = (R_{555} - R_{650})/(R_{555} + R_{650} - R_{475})$	(Gitelson *et al.*, 2001)
Visible Atmospherically Resistant Index 2	$VARI_2 = (R_{560} - R_{668})/(R_{560} + R_{668} - R_{475})$	(Gitelson *et al.*, 2001)
Anthocyanin Reflectance Index 1	$ARI_1 = 1/R_{550} - 1/R_{700}$	(Gitelson *et al.*, 2001)
Anthocyanin Reflectance Index 2	$ARI_2 = 1/R_{550} - 1/R_{700}$	(Gitelson *et al.*, 2002)
Modified Anthocyanin Reflectance Index	$mARI = R_{760:800}(1/R_{540:560} - 1/R_{690:710})$	(Gitelson *et al.*, 2006)
Modified Anthocyanin Reflectance Index 1	$ARI_1m = R_{760:800}(1/R_{550} - 1/R_{700})$	-
Modified Anthocyanin Reflectance Index 2	$ARI_1m_2 = R_{800}(1/R_{550} - 1/R_{700})$	-
Nitrogen		
Double-peak Canopy Nitrogen Index	$DCNI = (R_{720} - R_{700})/(R_{700} - R_{670})/(R_{720} - R_{670} + 0.03)$	(Chen *et al.*, 2010)
SWIR		
Gnyp and Li Index	$GnyLi = \frac{(R_{900}\ R_{1050}) - (R_{955}\ R_{1220})}{(R_{900}\ R_{1050}) + (R_{955}\ R_{1220})}$	(Gnyp *et al.*, 2014)
CI_1	$CI_1 = (R_{736} - R_{735})\ R_{990}\ /\ R_{720}$	(Bao *et al.*, 2013)
CI_2	$CI_2 = (R_{736} - R_{735})\ R_{900}\ /\ R_{720}$	(Bao *et al.*, 2013)
Modified Chlorophyll Absorption Ratio Index 1510	$MCARI_{1510} = ((R_{700} - R_{1510}) - 0.2(R_{700} - R_{550}))\left(\frac{R_{700}}{R_{1510}}\right)$	(Herrmann *et al.*, 2010)
Transformed Chlorophyll Absorption Ratio 1510	$TCARI_{1510} = 3\left((R_{700} - R_{1510}) - 0.2\ (R_{700} - R_{550})\frac{R_{700}}{R_{1510}}\right)$	(Herrmann *et al.*, 2010)
Optimized Soil-Adjusted Vegetation Index 1510	$OSAVI_{1510} = (1 + 0.16)\ \frac{R_{800} - R_{1510}}{R_{800} + R_{1510} + 0.16}$	(Herrmann *et al.*, 2010)
TCARI/OSAVI 1510	$T/O_{1510} = TCARI_{1510}\ OSAVI_{1510}$	(Herrmann *et al.*, 2010)
Normalized Ratio Index 1510	$NRI_{1510} = (R_{1510} - R_{660})/(R_{1510} + R_{660})$	(Herrmann *et al.*, 2010)
Ratio Spectral Index 990 720	$RSI_{990,720} = R_{990})/R_{720}$	(Yao *et al.*, 2010)
Normalized Ratio Index 1770	$NRI_{1770} = (R_{1770} - R_{693})/(R_{1770} + R_{693})$	(Ferwerda *et al.*, 2005)
Normalized Difference Nitrogen Index	$NDNI = \frac{\log_{10}(1/R_{1510}) - \log_{10}(1/R_{1680})}{\log_{10}(1/R_{1510}) + \log_{10}(1/R_{1680})}$	(Serrano *et al.*, 2002)
Sulphur index 1080	$S_{1080} = (R_{1080} - R_{660})/(R_{1080} + R_{660})$	(Mahajan *et al.*, 2014)
Sulphur index 1260	$S_{1260} = (R_{1260} - R_{660})/(R_{1260} + R_{660})$	(Mahajan *et al.*, 2014)
Normalized 1645 1715	$N_{1645,1715} = (R_{1645} - R_{1715})/(R_{1645} + R_{1715})$	(Pimstein *et al.*, 2011)
Normalized 870 1450	$N_{870,1450} = (R_{870} - R_{1450})/(R_{870} + R_{1450})$	(Pimstein *et al.*, 2011)
Normalized 850 1510	$N_{850,1510} = (R_{850} - R_{1510})/(R_{850} + R_{1510})$	(Camino *et al.*, 2018)
Middle-infrared Normalized Difference	$MND = (R_{1080} - R_{1675})/(R_{1080} + R_{1675})$	(Malthus *et al.*, 1993)
Normalized Difference Water Index	$NDWI = (R_{860} - R_{1240})/(R_{860} + R_{1240})$	(Gao, 1996)
Fluorescence		
3FLD	$3FLD = \frac{E_{out}\ \cdot\ L_{in} - E_{in} \cdot L_{out}}{E_{out} - E_{in}}$	(Maier *et al.*, 2003; Plascyk, 1975)

Appendix B.

Confusion matrix and statistics from the example predictions.

Prediction \ Observation	0	1
0	310	78
1	72	336

Accuracy	0.8116
Kappa	0.6227
95% Confidence Interval	(0.783, 0.838)
No-information rate	0.5201
Sensitivity	0.8115
Specificity	0.8116

References

Ahrens, C.W., Andrew, M.E., Mazanec, R.A., Ruthrof, K.X., Challis, A., Hardy, G., Byrne, M., Tissue, D.T., Rymer, P.D., 2020. Plant functional traits differ in adaptability and are predicted to be differentially affected by climate change. Ecology and Evolution 10, 232–248. https://doi.org/10.1002/ece3.5890

Badgley, G., Field, C.B., Berry, J.A., 2017. Canopy near-infrared reflectance and terrestrial photosynthesis. Sci Adv 3, e1602244. https://doi.org/10.1126/sciadv.1602244

Bao, Y., Xu, K., Min, J., Xu, J., 2013. Estimating Wheat Shoot Nitrogen Content at Vegetative Stage from In Situ Hyperspectral Measurements. Crop Science 53, 2063–2071. https://doi.org/10.2135/cropsci2013.01.0012

Baquedano, F.J., Castillo, F.J., 2007. Drought tolerance in the Mediterranean species Quercus coccifera, Quercus ilex, Pinus halepensis, and Juniperus phoenicea. Photosynthetica 45, 229. https://doi.org/10.1007/s11099-007-0037-x

Barnes, J.D., Balaguer, L., Manrique, E., Elvira, S., Davison, A.W., 1992. A reappraisal of the use of DMSO for the extraction and determination of chlorophylls a and b in lichens and higher plants. Environmental and Experimental Botany 32, 85–100. https://doi.org/10.1016/0098-8472(92)90034-Y

Blackburn, G.A., 1998. Spectral indices for estimating photosynthetic pigment concentrations: A test using senescent tree leaves. International Journal of Remote Sensing 19, 657–675. https://doi.org/10.1080/014311698215919

Breiman, L., 2001. Random Forests. Machine Learning 45, 5–32. https://doi.org/10.1023/A:1010933404324

Broge, N.H., Leblanc, E., 2001. Comparing prediction power and stability of broadband and hyperspectral vegetation indices for estimation of green leaf area index and canopy chlorophyll density. Remote Sensing of Environment 76, 156–172. https://doi.org/10.1016/S0034-4257(00)00197-8

Calderón, R., Navas-Cortés, J.A., Zarco-Tejada, P.J., 2015. Early Detection and Quantification of Verticillium Wilt in Olive Using Hyperspectral and Thermal Imagery over Large Areas. Remote Sensing 7, 5584–5610. https://doi.org/10.3390/rs70505584

Camarero, J.J., Olano, J.M., Arroyo Alfaro, S.J., Fernández-Marín, B., Becerril, J.M., García-Plazaola, J.I., 2012. Photoprotection mechanisms in Quercus ilex under contrasting climatic conditions. Flora - Morphology, Distribution, Functional Ecology of Plants 207, 557–564. https://doi.org/10.1016/j.flora.2012.06.003

Camilo-Alves, C. de S. e P., Clara, M.I.E. da, Ribeiro, N.M.C. de A., 2013. Decline of Mediterranean oak trees and its association with Phytophthora cinnamomi: a review. Eur J Forest Res 132, 411–432. https://doi.org/10.1007/s10342-013-0688-z

Camino, C., González-Dugo, V., Hernández, P., Sillero, J.C., Zarco-Tejada, P.J., 2018. Improved nitrogen retrievals with airborne-derived fluorescence and plant traits quantified from VNIR-SWIR hyperspectral imagery in the context of precision agriculture. International Journal of Applied Earth Observation and Geoinformation 70, 105–117. https://doi.org/10.1016/j.jag.2018.04.013

Carter, G.A., 1994. Ratios of leaf reflectances in narrow wavebands as indicators of plant stress. International Journal of Remote Sensing 15, 697–703. https://doi.org/10.1080/01431169408954109

Castrignano, A., Buttafuoco, G., Khosla, R., Mouazen, A., Moshou, D., Naud, O. (Eds.), 2020. Agricultural internet of things and decision support for precision smart farming, 1st ed. Elsevier, Cambridge.

Ceccato, P., Flasse, S., Tarantola, S., Jacquemoud, S., Grégoire, J.-M., 2001. Detecting vegetation leaf water content using reflectance in the optical domain. Remote Sensing of Environment 77, 22–33. https://doi.org/10.1016/S0034-4257(01)00191-2

Chappelle, E.W., Kim, M.S., McMurtrey, J.E., 1992. Ratio analysis of reflectance spectra (RARS): An algorithm for the remote estimation of the concentrations of chlorophyll A, chlorophyll B, and carotenoids in soybean leaves. Remote Sensing of Environment 39, 239–247. https://doi.org/10.1016/0034-4257(92)90089-3

Chen, J.M., 1996. Evaluation of Vegetation Indices and a Modified Simple Ratio for Boreal Applications. Canadian Journal of Remote Sensing 22, 229–242. https://doi.org/10.1080/07038992.1996.10855178

Chen, P., Haboudane, D., Tremblay, N., Wang, J., Vigneault, P., Li, B., 2010. New spectral indicator assessing the efficiency of crop nitrogen treatment in corn and wheat. Remote Sensing of Environment 114, 1987–1997. https://doi.org/10.1016/j.rse.2010.04.006

Cicchetti, D.V., Sparrow, S.A., 1981. Developing criteria for establishing interrater reliability of specific items: Applications to assessment of adaptive behavior. American Journal of Mental Deficiency 86, 127–137.

Cleveland, W.S., Grosse, E., Shyu, W.M., 1992. Local regression models. Statistical models in S 2, 309–376.

Colangelo, M., Camarero, J.J., Borghetti, M., Gentilesca, T., Oliva, J., Redondo, M.-A., Ripullone, F., 2018. Drought and Phytophthora Are Associated With the Decline of Oak Species in Southern Italy. Front. Plant Sci. 9. https://doi.org/10.3389/fpls.2018.01595

Combal, B., Baret, F., Weiss, M., Trubuil, A., Macé, D., Pragnère, A., Myneni, R., Knyazikhin, Y., Wang, L., 2003. Retrieval of canopy biophysical variables from bidirectional reflectance: Using prior information to solve the ill-posed inverse problem. Remote Sensing of Environment 84, 1–15. https://doi.org/10.1016/S0034-4257(02)00035-4

Consejería de Medio Ambiente y Ordenación del Territorio, 2018. Manual para el establecimiento y la evaluación de las parcelas de la Red Andaluza de Seguimiento de Daños sobre Ecosistemas Forestales: Red SEDA y Red de PINSAPO. Junta de Andalucía.

Corcobado, T., Cubera, E., Juárez, E., Moreno, G., Solla, A., 2014. Drought events determine performance of Quercus ilex seedlings and increase their susceptibility to Phytophthora cinnamomi. Agricultural and Forest Meteorology 192–193, 1–8. https://doi.org/10.1016/j.agrformet.2014.02.007

Corcobado, T., Solla, A., Madeira, M.A., Moreno, G., 2013. Combined effects of soil properties and Phytophthora cinnamomi infections on Quercus ilex decline. Plant Soil 373, 403–413. https://doi.org/10.1007/s11104-013-1804-z

Cunniffe, N.J., Cobb, R.C., Meentemeyer, R.K., Rizzo, D.M., Gilligan, C.A., 2016. Modeling when, where, and how to manage a forest epidemic, motivated by sudden oak death in California. PNAS 113, 5640–5645. https://doi.org/10.1073/pnas.1602153113

Datt, B., 1998. Remote Sensing of Chlorophyll a, Chlorophyll b, Chlorophyll a+b, and Total Carotenoid Content in Eucalyptus Leaves. Remote Sensing of Environment 66, 111–121. https://doi.org/10.1016/S0034-4257(98)00046-7

Dormann, C.F., Elith, J., Bacher, S., Buchmann, C., Carl, G., Carré, G., Marquéz, J.R.G., Gruber, B., Lafourcade, B., Leitão, P.J., Münkemüller, T., McClean, C., Osborne, P.E., Reineking, B., Schröder, B., Skidmore, A.K., Zurell, D., Lautenbach, S., 2013. Collinearity: a review of methods to deal with it and a simulation study evaluating their performance. Ecography 36, 27–46. https://doi.org/10.1111/j.1600-0587.2012.07348.x

Eichhorn, J., Roskams, P., Potočić, N., Timmermann, V., Ferretti, M., Mues, V., Szepesi, A., Durrant, D., Seletković, I., Schroeck, H.-W., Nevalnien, S., Filippo Bussotti, García, P., Wulff, S., 2017. Part IV: Visual assessment of crown condition and damaging agents., in: UNECE ICP Forests Programme Co-ordinating Centre. Manual on methods and criteria for harmonized sampling, assessment, monitoring and analysis of the effects of air pollution on forests. Thünen Institute of Forest Ecosystems, Eberswalde, Germany, p. 54.

Féret, J.-B., Gitelson, A.A., Noble, S.D., Jacquemoud, S., 2017. PROSPECT-D: Towards modeling leaf optical properties through a complete lifecycle. Remote Sensing of Environment 193, 204–215. https://doi.org/10.1016/j.rse.2017.03.004

Fernández i Marti, A., Romero-Rodríguez, C., Navarro-Cerrillo, R.M., Abril, N., Jorrín-Novo, J.V., Dodd, R.S., 2018. Population Genetic Diversity of Quercus ilex subsp. ballota (Desf.) Samp. Reveals Divergence in Recent and Evolutionary Migration Rates in the Spanish Dehesas. Forests 9, 337. https://doi.org/10.3390/f9060337

Ferwerda, J.G., Skidmore, A.K., Mutanga, O., 2005. Nitrogen detection with hyperspectral normalized ratio indices across multiple plant species. International Journal of Remote Sensing 26, 4083–4095. https://doi.org/10.1080/01431160500181044

Früchtenicht, E., Klein, N., Brüggemann, W., 2018. Response of Quercus robur and two potential climate change winners – Quercus pubescens and Quercus ilex – to two years summer drought in a semi-controlled competition study: II — Photosynthetic efficiency. Environmental and Experimental Botany, Experiments with trees: from seedlings to ecosystems 152, 118–127. https://doi.org/10.1016/j.envexpbot.2018.03.019

Gamon, J.A., Peñuelas, J., Field, C.B., 1992. A narrow-waveband spectral index that tracks diurnal changes in photosynthetic efficiency. Remote Sensing of Environment 41, 35–44. https://doi.org/10.1016/0034-4257(92)90059-S

Gao, B., 1996. NDWI—A normalized difference water index for remote sensing of vegetation liquid water from space. Remote Sensing of Environment 58, 257–266. https://doi.org/10.1016/S0034-4257(96)00067-3

Garrity, S.R., Eitel, J.U.H., Vierling, L.A., 2011. Disentangling the relationships between plant pigments and the photochemical reflectance index reveals a new approach for remote estimation of carotenoid content. Remote Sensing of Environment 115, 628–635. https://doi.org/10.1016/j.rse.2010.10.007

Gastellu-Etchegorry, J.P., Demarez, V., Pinel, V., Zagolski, F., 1996. Modeling radiative transfer in heterogeneous 3-D

vegetation canopies. Remote Sensing of Environment 58, 131–156. https://doi.org/10.1016/0034-4257(95)00253-7

Gigović, L., Pourghasemi, H.R., Drobnjak, S., Bai, S., 2019. Testing a New Ensemble Model Based on SVM and Random Forest in Forest Fire Susceptibility Assessment and Its Mapping in Serbia's Tara National Park. Forests 10, 408. https://doi.org/10.3390/f10050408

Gitelson, A., Merzlyak, M., Zur, Y., Stark, R., Gritz, U., 2001. Non-destructive and remote sensing techniques for estimation of vegetation status. Papers in Natural Resources.

Gitelson, A.A., Gritz †, Y., Merzlyak, M.N., 2003. Relationships between leaf chlorophyll content and spectral reflectance and algorithms for non-destructive chlorophyll assessment in higher plant leaves. Journal of Plant Physiology 160, 271–282. https://doi.org/10.1078/0176-1617-00887

Gitelson, A.A., Keydan, G.P., Merzlyak, M.N., 2006. Three-band model for noninvasive estimation of chlorophyll, carotenoids, and anthocyanin contents in higher plant leaves. Geophys. Res. Lett. 33, L11402. https://doi.org/10.1029/2006GL026457

Gitelson, A.A., Merzlyak, M.N., 1996. Signature Analysis of Leaf Reflectance Spectra: Algorithm Development for Remote Sensing of Chlorophyll. Journal of Plant Physiology 148, 494–500. https://doi.org/10.1016/S0176-1617(96)80284-7

Gitelson, A.A., Yacobi, Y.Z., Schalles, J.E., Rundquist, D.C., Han, L., Stark, R., Etzion, D., 2000. Remote Estimation of Phytoplankton Density in Productive Waters. Arch. HydrobioI. Spec. Issues Advanc. Limnol. Limnology and Lake Management 2000+ 55, 121–136.

Gitelson, A.A., Zur, Y., Chivkunova, O.B., Merzlyak, M.N., 2002. Assessing Carotenoid Content in Plant Leaves with Reflectance Spectroscopy. Photochemistry and Photobiology 75, 272–281. https://doi.org/10.1562/0031-8655(2002)0750272ACCIPL2.0.CO2

Gnyp, M.L., Bareth, G., Li, F., Lenz-Wiedemann, V.I.S., Koppe, W., Miao, Y., Hennig, S.D., Jia, L., Laudien, R., Chen, X., Zhang, F., 2014. Development and implementation of a multiscale biomass model using hyperspectral vegetation indices for winter wheat in the North China Plain. International Journal of Applied Earth Observation and Geoinformation 33, 232–242. https://doi.org/10.1016/j.jag.2014.05.006

Gonzalez-Dugo, V., Zarco-Tejada, P.J., Fereres, E., 2014. Applicability and limitations of using the crop water stress index as an indicator of water deficits in citrus orchards. Agricultural and Forest Meteorology 198–199, 94–104. https://doi.org/10.1016/j.agrformet.2014.08.003

Gonzalez-Dugo, V., Zarco-Tejada, P.J., Intrigliolo, D.S., Ramírez-Cuesta, J.-M., 2020. Normalization of the crop water stress index to assess the within-field spatial variability of water stress sensitivity. Precision Agric. https://doi.org/10.1007/s11119-020-09768-6

Gualtieri, A.G., Chettri, S., Cromp, R., Johnson, L., 1999. Support Vector Machine Classifiers as Applied to AVIRIS Data [WWW Document]. URL /paper/Support-Vector-Machine-Classifiers-as-Applied-to-Gualtieri-Chettri/83e3788925a7a78bcc89a4540c8808f8e2b7acb0 (accessed 11.16.20).

Gueymard, C., 1995. SMARTS2: a simple model of the atmospheric radiative transfer of sunshine: algorithms and performance assessment. Florida Solar Energy Center Cocoa, FL.

Gueymard, C.A., 2001. Parameterized transmittance model for direct beam and circumsolar spectral irradiance. Solar Energy 71, 325–346. https://doi.org/10.1016/S0038-092X(01)00054-8

Haboudane, D., Miller, J.R., Pattey, E., Zarco-Tejada, P.J., Strachan, I.B., 2004. Hyperspectral vegetation indices and novel algorithms for predicting green LAI of crop canopies: Modeling and validation in the context of precision agriculture. Remote Sensing of Environment 90, 337–352. https://doi.org/10.1016/j.rse.2003.12.013

Haboudane, D., Miller, J.R., Tremblay, N., Zarco-Tejada, P.J., Dextraze, L., 2002. Integrated narrow-band vegetation indices for prediction of crop chlorophyll content for application to precision agriculture. Remote Sensing of Environment 81, 416–426. https://doi.org/10.1016/S0034-4257(02)00018-4

Harrower, M., Brewer, C.A., 2003. ColorBrewer. org: an online tool for selecting colour schemes for maps. The Cartographic Journal 40, 27–37.

Haynes, W., 2013. Bonferroni Correction, in: Encyclopedia of Systems Biology. Springer, New York, NY, pp. 154–154. https://doi.org/10.1007/978-1-4419-9863-7_1213

Hernández-Clemente, R., Hornero, A., Mottus, M., Penuelas, J., González-Dugo, V., Jiménez, J.C., Suárez, L., Alonso, L., Zarco-Tejada, P.J., 2019. Early Diagnosis of Vegetation Health From High-Resolution Hyperspectral and Thermal Imagery: Lessons Learned From Empirical Relationships and Radiative Transfer Modelling. Curr Forestry Rep 5, 169–183. https://doi.org/10.1007/s40725-019-00096-1

Hernández-Clemente, R., Navarro-Cerrillo, R.M., Suárez, L., Morales, F., Zarco-Tejada, P.J., 2011. Assessing structural effects on PRI for stress detection in conifer forests. Remote Sensing of Environment 115, 2360–2375. https://doi.org/10.1016/j.rse.2011.04.036

Hernández-Clemente, R., Navarro-Cerrillo, R.M., Zarco-Tejada, P.J., 2012. Carotenoid content estimation in a heterogeneous conifer forest using narrow-band indices and PROSPECT+DART simulations. Remote Sensing of Environment 127, 298–315. https://doi.org/10.1016/j.rse.2012.09.014

Hernández-Clemente, R., North, P.R.J., Hornero, A., Zarco-Tejada, P.J., 2017. Assessing the effects of forest health

on sun-induced chlorophyll fluorescence using the FluorFLIGHT 3-D radiative transfer model to account for forest structure. Remote Sensing of Environment 193, 165–179. https://doi.org/10.1016/j.rse.2017.02.012

Herrmann, I., Karnieli, A., Bonfil, D.J., Cohen, Y., Alchanatis, V., 2010. SWIR-based spectral indices for assessing nitrogen content in potato fields. International Journal of Remote Sensing 31, 5127–5143. https://doi.org/10.1080/01431160903283892

Homolová, L., Malenovský, Z., Clevers, J.G.P.W., García-Santos, G., Schaepman, M.E., 2013. Review of optical-based remote sensing for plant trait mapping. Ecological Complexity 15, 1–16. https://doi.org/10.1016/j.ecocom.2013.06.003

Hornero, A., Hernández-Clemente, R., North, P.R.J., Beck, P.S.A., Boscia, D., Navas-Cortes, J.A., Zarco-Tejada, P.J., 2020. Monitoring the incidence of Xylella fastidiosa infection in olive orchards using ground-based evaluations, airborne imaging spectroscopy and Sentinel-2 time series through 3-D radiative transfer modelling. Remote Sensing of Environment 236, 111480. https://doi.org/10.1016/j.rse.2019.111480

Hornero, A., North, P.R.J., Zarco-Tejada, P.J., Rascher, U., Martín, M.P., Migliavacca, M., Hernandez-Clemente, R., 2021. Assessing the contribution of understory sun-induced chlorophyll fluorescence through 3-D radiative transfer modelling and field data. Remote Sensing of Environment 253, 112195. https://doi.org/10.1016/j.rse.2020.112195

Huete, A., Didan, K., Miura, T., Rodriguez, E.P., Gao, X., Ferreira, L.G., 2002. Overview of the radiometric and biophysical performance of the MODIS vegetation indices. Remote Sensing of Environment, The Moderate Resolution Imaging Spectroradiometer (MODIS): a new generation of Land Surface Monitoring 83, 195–213. https://doi.org/10.1016/S0034-4257(02)00096-2

Hutchings, M., John, E., Stewart, A., 2000. The Ecological Consequences of Environmental Heterogeneity: 40th Symposium of the British Ecological Society.

James, G., Witten, D., Hastie, T., Tibshirani, R., 2013. Classification, in: James, G., Witten, D., Hastie, T., Tibshirani, R. (Eds.), An Introduction to Statistical Learning: With Applications in R, Springer Texts in Statistics. Springer, New York, NY, pp. 127–173. https://doi.org/10.1007/978-1-4614-7138-7_4

Jordan, C.F., 1969. Derivation of Leaf-Area Index from Quality of Light on the Forest Floor. Ecology 50, 663–666. https://doi.org/10.2307/1936256

Jung, T., Blaschke, H., Osswald, W., 2000. Involvement of soilborne *Phytophthora* species in Central European oak decline and the effect of site factors on the disease. Plant Pathology 49, 706–718. https://doi.org/10.1046/j.1365-3059.2000.00521.x

Kattenborn, T., Fassnacht, F.E., Pierce, S., Lopatin, J., Grime, J.P., Schmidtlein, S., 2017. Linking plant strategies and plant traits derived by radiative transfer modelling. J Veg Sci 28, 717–727. https://doi.org/10.1111/jvs.12525

Koller, S., Holland, V., Brüggemann, W., 2013. Effects of drought stress on the evergreen Quercus ilex L., the deciduous Q. robur L. and their hybrid Q. × turneri Willd. Photosynthetica 51, 574–582. https://doi.org/10.1007/s11099-013-0058-6

Kötz, B., Schaepman, M., Morsdorf, F., Bowyer, P., Itten, K., Allgöwer, B., 2004. Radiative transfer modeling within a heterogeneous canopy for estimation of forest fire fuel properties. Remote Sensing of Environment, Forest Fire Prevention and Assessment 92, 332–344. https://doi.org/10.1016/j.rse.2004.05.015

Kursa, M.B., Rudnicki, W.R., 2010. Feature Selection with the Boruta Package. Journal of Statistical Software 36, 1–13. https://doi.org/10.18637/jss.v036.i11

Lee, J., Rennaker, C., Wrolstad, R.E., 2008. Correlation of two anthocyanin quantification methods: HPLC and spectrophotometric methods. Food Chemistry 110, 782–786. https://doi.org/10.1016/j.foodchem.2008.03.010

Liaw, A., Wiener, M., 2002. Classification and Regression by randomForest. R News 2, 18–22.

Lichtenthaler, H.K., 1996. Vegetation Stress: an Introduction to the Stress Concept in Plants. Journal of Plant Physiology 148, 4–14. https://doi.org/10.1016/S0176-1617(96)80287-2

Liu, P., Choo, K.-K.R., Wang, L., Huang, F., 2017. SVM or deep learning? A comparative study on remote sensing image classification. Soft Comput 21, 7053–7065. https://doi.org/10.1007/s00500-016-2247-2

Liu, W., Luo, S., Lu, X., Atherton, J., Gastellu-Etchegorry, J.-P., 2020. Simulation-Based Evaluation of the Estimation Methods of Far-Red Solar-Induced Chlorophyll Fluorescence Escape Probability in Discontinuous Forest Canopies. Remote Sensing 12, 3962. https://doi.org/10.3390/rs12233962

López-López, M., Calderón, R., González-Dugo, V., Zarco-Tejada, P.J., Fereres, E., 2016. Early Detection and Quantification of Almond Red Leaf Blotch Using High-Resolution Hyperspectral and Thermal Imagery. Remote Sensing 8, 276. https://doi.org/10.3390/rs8040276

Mahajan, G.R., Sahoo, R.N., Pandey, R.N., Gupta, V.K., Kumar, D., 2014. Using hyperspectral remote sensing techniques to monitor nitrogen, phosphorus, sulphur and potassium in wheat (Triticum aestivum L.). Precision Agric 15, 499–522. https://doi.org/10.1007/s11119-014-9348-7

Mahlein, A.-K., Rumpf, T., Welke, P., Dehne, H.-W., Plümer, L., Steiner, U., Oerke, E.-C., 2013. Development of spectral indices for detecting and identifying plant diseases. Remote Sensing of Environment 128, 21–30. https://doi.org/10.1016/j.rse.2012.09.019

Maier, S.W., Günther, K.P., Stellmes, M., 2003. Sun-Induced Fluorescence: A New Tool for Precision Farming.

Digital Imaging and Spectral Techniques: Applications to Precision Agriculture and Crop Physiology asaspecialpubli, 209–222. https://doi.org/10.2134/asaspecpub66.c16

Malthus, T.J., Andrieu, B., Danson, F.M., Jaggard, K.W., Steven, M.D., 1993. Candidate high spectral resolution infrared indices for crop cover. Remote Sensing of Environment 46, 204–212. https://doi.org/10.1016/0034-4257(93)90095-F

Manion, P.D., Lachance, D., 1992. Forest Decline Concepts. APS Press.

Markiet, V., Perheentupa, V., Mõttus, M., Hernández-Clemente, R., 2016. Usability of multiangular imaging spectroscopy data for analysis of vegetation canopy shadow fraction in boreal forest, in: Mapping, Monitoring & Modelling of Vegetation Characteristics Using Earth Observation. Presented at the EGU General Assembly Conference Abstracts, Ask, M. et al., Vienna, Austria., p. 14399.

Merzlyak, M.N., Gitelson, A.A., Chivkunova, O.B., Rakitin, V.YU., 1999. Non-destructive optical detection of pigment changes during leaf senescence and fruit ripening. Physiologia Plantarum 106, 135–141. https://doi.org/10.1034/j.1399-3054.1999.106119.x

Mohammed, G.H., Colombo, R., Middleton, E.M., Rascher, U., van der Tol, C., Nedbal, L., Goulas, Y., Pérez-Priego, O., Damm, A., Meroni, M., Joiner, J., Cogliati, S., Verhoef, W., Malenovský, Z., Gastellu-Etchegorry, J.-P., Miller, J.R., Guanter, L., Moreno, J., Moya, I., Berry, J.A., Frankenberg, C., Zarco-Tejada, P.J., 2019. Remote sensing of solar-induced chlorophyll fluorescence (SIF) in vegetation: 50 years of progress. Remote Sensing of Environment 231, 111177. https://doi.org/10.1016/j.rse.2019.04.030

Moralejo, E., García-Muñoz, J.A., Descals, E., 2009. Susceptibility of Iberian trees to Phytophthora ramorum and P. cinnamomi. Plant Pathology 58, 271–283. https://doi.org/10.1111/j.1365-3059.2008.01956.x

Murray, J.R., Hackett, W.P., 1991. Dihydroflavonol Reductase Activity in Relation to Differential Anthocyanin Accumulation in Juvenile and Mature Phase Hedera helix L. Plant Physiol 97, 343–351. https://doi.org/10.1104/pp.97.1.343

Navarro-Cerrillo, R.M., Ruiz Gómez, F.J., Cabrera-Puerto, R.J., Sánchez-Cuesta, R., Palacios Rodriguez, G., Quero Pérez, J.L., 2018. Growth and physiological sapling responses of eleven Quercus ilex ecotypes under identical environmental conditions. Forest Ecology and Management 415–416, 58–69. https://doi.org/10.1016/j.foreco.2018.01.004

North, P.R.J., 1996. Three-dimensional forest light interaction model using a Monte Carlo method. IEEE Transactions on Geoscience and Remote Sensing 34, 946–956. https://doi.org/10.1109/36.508411

Pal, M., 2005. Random forest classifier for remote sensing classification. International Journal of Remote Sensing 26, 217–222. https://doi.org/10.1080/01431160412331269698

Penuelas, J., Frederic, B., Filella, I., 1995. Semi-Empirical Indices to Assess Carotenoids/Chlorophyll-a Ratio from Leaf Spectral Reflectance.

Pimstein, A., Karnieli, A., Bansal, S.K., Bonfil, D.J., 2011. Exploring remotely sensed technologies for monitoring wheat potassium and phosphorus using field spectroscopy. Field Crops Research 121, 125–135. https://doi.org/10.1016/j.fcr.2010.12.001

Pisek, J., Lang, M., Kuusk, J., 2015. A note on suitable viewing configuration for retrieval of forest understory reflectance from multi-angle remote sensing data. Remote Sensing of Environment 156, 242–246. https://doi.org/10.1016/j.rse.2014.09.033

Plascyk, J.A., 1975. The MK II Fraunhofer Line Discriminator (FLD-II) for Airborne and Orbital Remote Sensing of Solar-Stimulated Luminescence. OE, OPEGAR 14, 144339. https://doi.org/10.1117/12.7971842

Qi, J., Chehbouni, A., Huete, A.R., Kerr, Y.H., Sorooshian, S., 1994. A modified soil adjusted vegetation index. Remote Sensing of Environment 48, 119–126. https://doi.org/10.1016/0034-4257(94)90134-1

REDIAM, Junta de Andalucía, 2021. Andalusian Environmental Information Network (REDIAM). Regional Ministry website. Junta de Andalucía [WWW Document]. URL http://www.juntadeandalucia.es/medioambiente/site/rediam (accessed 1.9.21).

Richards, J.A., Jia, X., 1999. Remote Sensing Digital Image Analysis: An Introduction, 3rd ed. Springer-Verlag, Berlin Heidelberg. https://doi.org/10.1007/978-3-662-03978-6

Roberts, O., Bunting, P., Hardy, A., McInerney, D., 2020. Sensitivity Analysis of the DART Model for Forest Mensuration with Airborne Laser Scanning. Remote Sensing 12, 247. https://doi.org/10.3390/rs12020247

Rocha, A.D., Groen, T.A., Skidmore, A.K., 2019. Spatially-explicit modelling with support of hyperspectral data can improve prediction of plant traits. Remote Sensing of Environment 231, 111200. https://doi.org/10.1016/j.rse.2019.05.019

Romero, M.A., González, M., Serrano, M.S., Sánchez, M.E., 2019. Trunk injection of fosetyl-aluminium controls the root disease caused by Phytophthora cinnamomi on Quercus ilex woodlands. Annals of Applied Biology 174, 313–318. https://doi.org/10.1111/aab.12503

Rondeaux, G., Steven, M., Baret, F., 1996. Optimization of soil-adjusted vegetation indices. Remote Sensing of Environment 55, 95–107. https://doi.org/10.1016/0034-4257(95)00186-7

Roujean, J.-L., Breon, F.-M., 1995. Estimating PAR absorbed by vegetation from bidirectional reflectance measurements. Remote Sensing of Environment 51, 375–384. https://doi.org/10.1016/0034-4257(94)00114-3

Rouse, J.W., Jr., Haas, R.H., Schell, J.A., Deering, D.W., 1974. Monitoring Vegetation Systems in the Great Plains with Erts. NASA Special Publication 351, 309.

Ruiz Gómez, F.J., Pérez-de-Luque, A., Sánchez-Cuesta, R., Quero, J.L., Navarro Cerrillo, R.M., 2018. Differences in the Response to Acute Drought and Phytophthora cinnamomi Rands Infection in Quercus ilex L. Seedlings. Forests 9, 634. https://doi.org/10.3390/f9100634

Ruiz-Gómez, F.J., Navarro-Cerrillo, R.M., Oβwald, W., Vannini, A., Morales-Rodriguez, C., 2019. Assessment of functional and structural changes of soil fungal and oomycete communities in holm oak declined dehesas through metabarcoding analysis. Scientific Reports 9, 5315. https://doi.org/10.1038/s41598-019-41804-y

San, B.T., Süzen, M.L., 2011. Evaluation of cross-track illumination in EO-1 Hyperion imagery for lithological mapping. International Journal of Remote Sensing 32, 7873–7889. https://doi.org/10.1080/01431161.2010.532175

Scholkopf, B., Kah-Kay Sung, Burges, C.J.C., Girosi, F., Niyogi, P., Poggio, T., Vapnik, V., 1997. Comparing support vector machines with Gaussian kernels to radial basis function classifiers. IEEE Transactions on Signal Processing 45, 2758–2765. https://doi.org/10.1109/78.650102

Seem, R.C., 1984. Disease Incidence and Severity Relationships. Annual Review of Phytopathology 22, 133–150. https://doi.org/10.1146/annurev.py.22.090184.001025

Serrano, L., Peñuelas, J., Ustin, S.L., 2002. Remote sensing of nitrogen and lignin in Mediterranean vegetation from AVIRIS data: Decomposing biochemical from structural signals. Remote Sensing of Environment 81, 355–364. https://doi.org/10.1016/S0034-4257(02)00011-1

Sims, D.A., Gamon, J.A., 2002. Relationships between leaf pigment content and spectral reflectance across a wide range of species, leaf structures and developmental stages. Remote Sensing of Environment 81, 337–354. https://doi.org/10.1016/S0034-4257(02)00010-X

Steele, M.R., Gitelson, A.A., Rundquist, D.C., Merzlyak, M.N., 2009. Nondestructive Estimation of Anthocyanin Content in Grapevine Leaves. Am J Enol Vitic. 60, 87–92.

Strang, G., Nguyen, T., 1996. Wavelets and Filter Banks. SIAM.

Suarez, L., González-Dugo, V., Camino, C., Hornero, A., Zarco-Tejada, P.J., 2021. Physical model inversion of the green spectral region to track assimilation rate in almond trees with an airborne nano-hyperspectral imager. Remote Sensing of Environment 252, 112147. https://doi.org/10.1016/j.rse.2020.112147

Trumbore, S., Brando, P., Hartmann, H., 2015. Forest health and global change. Science 349, 814–818. https://doi.org/10.1126/science.aac6759

Vilfan, N., van der Tol, C., Muller, O., Rascher, U., Verhoef, W., 2016. Fluspect-B: A model for leaf fluorescence, reflectance and transmittance spectra. https://doi.org/10.1016/j.rse.2016.09.017

Vogelmann, T.C., 1993. Plant Tissue Optics. Annu. Rev. Plant. Physiol. Plant. Mol. Biol. 44, 231–251. https://doi.org/10.1146/annurev.pp.44.060193.001311

Yao, X., Zhu, Y., Tian, Y., Feng, W., Cao, W., 2010. Exploring hyperspectral bands and estimation indices for leaf nitrogen accumulation in wheat. International Journal of Applied Earth Observation and Geoinformation 12, 89–100. https://doi.org/10.1016/j.jag.2009.11.008

Zarco-Tejada, P.J., Camino, C., Beck, P.S.A., Calderon, R., Hornero, A., Hernández-Clemente, R., Kattenborn, T., Montes-Borrego, M., Susca, L., Morelli, M., Gonzalez-Dugo, V., North, P.R.J., Landa, B.B., Boscia, D., Saponari, M., Navas-Cortes, J.A., 2018. Previsual symptoms of Xylella fastidiosa infection revealed in spectral plant-trait alterations. Nature Plants. https://doi.org/10.1038/s41477-018-0189-7

Zarco-Tejada, P.J., González-Dugo, V., Berni, J.A.J., 2012. Fluorescence, temperature and narrow-band indices acquired from a UAV platform for water stress detection using a micro-hyperspectral imager and a thermal camera. Remote Sensing of Environment, Remote Sensing of Urban Environments 117, 322–337. https://doi.org/10.1016/j.rse.2011.10.007

Zarco-Tejada, P.J., Miller, J.R., Mohammed, G.H., Noland, T.L., 2000. Chlorophyll Fluorescence Effects on Vegetation Apparent Reflectance: I. Leaf-Level Measurements and Model Simulation. Remote Sensing of Environment 74, 582–595. https://doi.org/10.1016/S0034-4257(00)00148-6

Zarco-Tejada, P.J., Miller, J.R., Mohammed, G.H., Noland, T.L., Sampson, P.H., 2001. Estimation of chlorophyll fluorescence under natural illumination from hyperspectral data. International Journal of Applied Earth Observation and Geoinformation 3, 321–327. https://doi.org/10.1016/S0303-2434(01)85039-X

Zarco-Tejada, P.J., Morales, A., Testi, L., Villalobos, F.J., 2013. Spatio-temporal patterns of chlorophyll fluorescence and physiological and structural indices acquired from hyperspectral imagery as compared with carbon fluxes measured with eddy covariance. Remote Sensing of Environment 133, 102–115. https://doi.org/10.1016/j.rse.2013.02.003

Zarco-Tejada, P.J., Whiting, M., Ustin, S., 2005. Temporal and Spatial Relationships between Within-Field Yield Variability in Cotton and High-Spatial Hyperspectral Remote Sensing Imagery. Agronomy journal 97. https://doi.org/10.2134/agronj2003.0257